REPORT DOCUMENTATION PAGE

Form Approved
OMB No. 0704-0188

1. AGENCY USE ONLY *(Leave blank)*	2. REPORT DATE Aug 96	3. REPORT TYPE AND DATES COVERED

4. TITLE AND SUBTITLE

The Interaction Between Downslope Flow and Trade-Wind Showers Over The Island of Hawaii During 7-8 August, 1990

5. FUNDING NUMBERS

6. AUTHOR(S)

Jeffrey L. Frye

7. PERFORMING ORGANIZATION NAME(S) AND ADDRESS(ES)

University of Hawaii

8. PERFORMING ORGANIZATION REPORT NUMBER

96-064

9. SPONSORING/MONITORING AGENCY NAME(S) AND ADDRESS(ES)

DEPARTMENT OF THE AIR FORCE
AFIT/CI
2950 P STEET, BLDG 125
WRIGHT-PATTERSON AFB OH 45433-7765

10. SPONSORING/MONITORING AGENCY REPORT NUMBER

11. SUPPLEMENTARY NOTES

12a. DISTRIBUTION/AVAILABILITY STATEMENT

Unlimited

12b. DISTRIBUTION CODE

13. ABSTRACT *(Maximum 200 words)*

14. SUBJECT TERMS

15. NUMBER OF PAGES
92

16. PRICE CODE

17. SECURITY CLASSIFICATION OF REPORT	18. SECURITY CLASSIFICATION OF THIS PAGE	19. SECURITY CLASSIFICATION OF ABSTRACT	20. LIMITATION OF ABSTRACT

GENERAL INSTRUCTIONS FOR COMPLETING SF 298

The Report Documentation Page (RDP) is used in announcing and cataloging reports. It is important that this information be consistent with the rest of the report, particularly the cover and title page. Instructions for filling in each block of the form follow. It is important to *stay within the lines* to meet *optical scanning requirements*.

Block 1. Agency Use Only *(Leave blank)*.

Block 2. Report Date. Full publication date including day, month, and year, if available (e.g. 1 Jan 88). Must cite at least the year.

Block 3. Type of Report and Dates Covered. State whether report is interim, final, etc. If applicable, enter inclusive report dates (e.g. 10 Jun 87 - 30 Jun 88).

Block 4. Title and Subtitle. A title is taken from the part of the report that provides the most meaningful and complete information. When a report is prepared in more than one volume, repeat the primary title, add volume number, and include subtitle for the specific volume. On classified documents enter the title classification in parentheses.

Block 5. Funding Numbers. To include contract and grant numbers; may include program element number(s), project number(s), task number(s), and work unit number(s). Use the following labels:

C	-	Contract	**PR**	- Project
G	-	Grant	**TA**	- Task
PE	-	Program Element	**WU**	- Work Unit Accession No.

Block 6. Author(s). Name(s) of person(s) responsible for writing the report, performing the research, or credited with the content of the report. If editor or compiler, this should follow the name(s).

Block 7. Performing Organization Name(s) and Address(es). Self-explanatory.

Block 8. Performing Organization Report Number. Enter the unique alphanumeric report number(s) assigned by the organization performing the report.

Block 9. Sponsoring/Monitoring Agency Name(s) and Address(es). Self-explanatory.

Block 10. Sponsoring/Monitoring Agency Report Number. *(If known)*

Block 11. Supplementary Notes. Enter information not included elsewhere such as: Prepared in cooperation with...; Trans. of...; To be published in.... When a report is revised, include a statement whether the new report supersedes or supplements the older report.

Block 12a. Distribution/Availability Statement. Denotes public availability or limitations. Cite any availability to the public. Enter additional limitations or special markings in all capitals (e.g. NOFORN, REL, ITAR).

DOD	-	See DoDD 5230.24, "Distribution Statements on Technical Documents."
DOE	-	See authorities.
NASA	-	See Handbook NHB 2200.2.
NTIS	-	Leave blank.

Block 12b. Distribution Code.

DOD	-	Leave blank.
DOE	-	Enter DOE distribution categories from the Standard Distribution for Unclassified Scientific and Technical Reports.
NASA	-	Leave blank.
NTIS	-	Leave blank.

Block 13. Abstract. Include a brief *(Maximum 200 words)* factual summary of the most significant information contained in the report.

Block 14. Subject Terms. Keywords or phrases identifying major subjects in the report.

Block 15. Number of Pages. Enter the total number of pages.

Block 16. Price Code. Enter appropriate price code *(NTIS only)*.

Blocks 17. - 19. Security Classifications. Self-explanatory. Enter U.S. Security Classification in accordance with U.S. Security Regulations (i.e., UNCLASSIFIED). If form contains classified information, stamp classification on the top and bottom of the page.

Block 20. Limitation of Abstract. This block must be completed to assign a limitation to the abstract. Enter either UL (unlimited) or SAR (same as report). An entry in this block is necessary if the abstract is to be limited. If blank, the abstract is assumed to be unlimited.

THE INTERACTION BETWEEN DOWNSLOPE FLOW AND TRADE-WIND

SHOWERS OVER THE ISLAND OF HAWAII DURING 7-8 AUGUST, 1990

A THESIS SUBMITTED TO THE GRADUATE DIVISION OF THE UNIVERSITY
OF HAWAII IN PARTIAL FULFILLMENT OF THE REQUIREMENTS FOR THE
DEGREE OF

MASTER OF SCIENCE

IN

METEOROLOGY

AUGUST 1996

19961212 032

By

Jeffrey L. Frye

Thesis Committee:

Yi-Leng Chen, Chairperson
Thomas Schroeder
Anders Daniels

ACKNOWLEDGMENTS

ABSTRACT

Data from the Hawaiian Rainband Project (HaRP) are used to study the interaction between downslope flow and trade-wind showers over windward sections of the island of Hawaii on 7-8 August 1990. Large-scale conditions produce strong upstream trade-winds of 11 m s^{-1} which are among the strongest observed during HaRP. In addition, frequent trade-wind showers are responsible for the largest precipitation accumulation between 0300-0700 HST over windward Hawaii during HaRP. The evolution of downslope flow and its interaction with the trade-wind showers under these conditions will be studied in detail.

The initiation of downslope flow occurs under dry conditions on the upper slopes by radiative cooling, and then progresses downslope until it arrives over windward lowlands. Here the downslope flow transition is held up by the strong trade winds occurring at the coast. Downslope flow is finally observed over the coast only after a band of rainshowers produces evaporative cooling allowing downslope winds to extend offshore. The evolution of downslope flow afterwards is affected by rainshowers. Vertical mixing associated with rainshowers transports trade-wind momentum into the weak downslope flow layer, replacing westerly winds with strong easterly winds. At the surface, a clear increase in temperature and moist static energy is observed as potentially warmer air aloft mixes with the surface layer. This temporary destruction of downslope flow produces an oscillation of the drainage front from 5-8 km offshore to 10 km inland.

There is also an interaction between downslope flow and trade winds along the drainage front. Radar reflectivity scans reveal enhancement and focusing of trade-wind showers as they encounter the drainage front. The radar data also confirms that most rainfall for the 7-8 August 1990 case is from preexisting showers that drift over the island.

TABLE OF CONTENTS

LIST OF FIGURES

LIST OF ABBREVIATIONS AND SYMBOLS

C   centigrade

dBZ   decibel

Fr   Froude Number

g   gravity

h   moist static energy

HaRP   Hawaiian Rainband Project

hPa   hectopascal

HST   Hawaiian Standard Time

km   kilometer

L   latent heat of vaporization

m   meter

Mhz   megahertz

mm   millimeter

N   Brunt-Vasala frequency

P   Pressure

PAM   Portable automated mesonet

q   specific humidity

T   temperature

U   zonal wind speed in the upstream region

u   zonal wind component

z   height

CHAPTER ONE

INTRODUCTION

1.1 Background

The largest island in the Hawaiian chain, Hawaii is dominated by two volcanic mountains exceeding 4 km in elevation, well above the typical height of the trade-wind inversion (approximately 2.2 km). The nearly continuous exposure to easterly trade winds in the summer months makes the island ideal for studying the interaction between atmosphere, ocean, and land processes. Such processes produce airflow and precipitation patterns that vary widely over the island due to the effects of orographic lifting, dynamic blocking, and thermally driven circulations.

The Hawaiian Rainband Project (HaRP) was conducted during July-August 1990 over the island of Hawaii to better understand the interaction between steady trade-wind flow and an island obstacle. It is the first time that comprehensive, high-quality datasets were collected by advanced instruments over a subtropical island. During HaRP, high resolution datasets were collected from 50 National Center for Atmospheric Research (NCAR) Portable Automated Mesonet (PAM) stations, research aircraft (NCAR Electra), tethersondes, rawinsondes, a National Oceanic and Atmospheric Administration (NOAA) boundary layer wind profiler, and a dual-Doppler network (NCAR CP-3 and CP-4) on the windward side of the island (Fig. 1.1). These datasets document the diurnal evolution of airflow and precipitation over the island, especially the windward side where interaction with prevailing trade wind-flow is the most dramatic. One of the major goals of HaRP was to document the structure and evolution of rainbands frequently observed along the

1

windward coast during the morning hours. Of particular interest was the investigation into the genesis of the rainbands and how it relates to dynamic effects and thermally generated circulations.

1.2 Previous studies

Observational studies prior to HaRP highlighted thermally forced airflow and its interaction with the prevailing trade winds. Leopold (1949) first described the splitting of winds around the island due to the trade-wind inversion. He described the trade-wind inversion as a "lid" forcing trade-wind flow to move around the island rather than over it. He described daytime conditions over windward locations dominated by orographic cloudiness by the combination of the trade-winds and sea breeze. At night, clear skies are observed as a land breeze develops eventually meeting the incoming trade winds to create a band of cloudiness offshore.

Garrett (1980) conducted an observational study of the flow pattern over the eastern slopes of Mauna Loa. He combined previous work from other researchers (Leopold, 1949, Eber 1957, Lavoie 1967, and Mendonca 1969) with his observations from a Hilo to Mauna Loa transect to form a conceptual model which relates island circulations to synoptic-scale winds. Garrett cites Leopold when describing the effect of the trade wind inversion on the trade winds, causing them to split around the island. He describes the daytime regime as first being triggered by differential heating rates over land and sea which results in a combined anabatic and sea breeze wind. In this situation, peak cloudiness and precipitation is found below the inversion somewhere upslope. It night, the situation reverses, with a thermally forced downslope wind at peak strength just before sunrise. The

drainage wind dissipates all the orographic cloud during the night. In his conceptual model, Garrett describes the shallow downslope flow meeting the incoming trade winds well offshore creating a convergence zone. This convergence zone has been attributed to forming the famous cloud bands offshore of Hilo.

In contrast to the early observational efforts, the modeling studies of Smolarkiewicz et al. (1988) and Rasmussen et al. (1989), describe the development of downslope flow and the observed nature of precipitation as the interaction between a strongly stratified fluid moving over a mountain barrier. They employ a numerical model using the Froude number (Fr = U/Nh, where U is the upstream wind speed, N is the Brunt-Vasala frequency, and h is the height of the barrier) to describe the airflow and mountain barrier. For typical trade-wind values (7.5 m s^{-1}), the Froude number is between 0.2-0.5, indicating that the flow lacks the energy to move over the barrier and must split and go around. On the upwind side of the island, the low-level winds are predicted to reverse direction due to a eastward directed pressure gradient induced by the interaction of the trade winds with the island. A convergence zone is created where the reverse flow encounters the trade winds resulting in the genesis region for the Hilo cloud bands. The modeling studies describe the flow reversal as dynamically induced due to the island barrier effect, and does not require a density current to create the downslope flow. More recent studies by Rasmussen and Smolarkiewicz (1993), however, have described the importance of thermal forcing in modulating the strength and depth of the downslope flow. They maintain, however, that the convergence zone is unaffected by nocturnal cooling and is completely determined by dynamic factors.

Analysis of the HaRP data supports thermal forcing of the mesoscale circulations. Chen and Nash (1994) presented a detailed analysis of the PAM data that described the

3

diurnal heating cycle as the modulator of surface airflow and precipitation occurrence. They found a distinct island-wide daytime upslope and nighttime downslope regime with short transitions in between. They also noted that observed rainfall frequencies are related to terrain and local winds. They describe windward rainfall as a complex interaction of orographic lifting, thermal forcing, and dynamic blocking. During the afternoon hours, most rainfall falls on the windward slopes due to orographic lifting by the combined upslope flow and trade winds. During the early evening hours, the rainfall begins to shift toward the coast. Here the rain begins in situ over the windward lowlands due to interaction with the katabatic flow and the incoming trade winds. As the evening continues, the rains shift to coastal areas as the downslope flow becomes more developed.

Chen and Wang (1994) presented data on the diurnal variation of surface thermodynamic fields. They noted that variations in surface temperature and dew point were related to orography, surface airflow, and distributions of cloudiness and rainfall. They further found that the onset of upslope flow is closely related to the thermal contrast between slope surface and surrounding environmental air at the same elevation. Upslope flow will begin when the virtual temperature at the surface first becomes warmer than its surroundings. They also describe the role of precipitation on the evolution of the downslope flow. They suggest radiative cooling can be reinforced by the evaporation of falling raindrops thereby strengthening the flow.

Chen and Wang (1995) used aircraft, tethersonde, and PAM station data to investigate the effects of precipitation on airflow over the island. They divided events into dry and wet cases and contrasted the differences. It was found that during the morning transition, rain cases showed higher surface temperature than dry cases along the slopes. This is attributed to widespread cloud cover reducing the outgoing longwave radiation and

4

downdrafts bringing warmer air above the nocturnal inversion to the surface. This results in a weaker (stronger) downslope flow during wet (dry) events. It was also found that rain and clouds can affect the timing of the wind shifts from downslope (upslope) to upslope (downslope) flow in the early morning (late afternoon). For example, wet cases have a later transition to upslope flow after sunrise due to less insolation and the evaporative cooling of falling raindrops. This is most pronounced near Hilo where precipitation frequency is large.

Wang and Chen (1995) take a detailed look at near-surface winds and thermal profiles during the transition periods between downslope and upslope flow. They suggest that the downslope flow just before sunrise is characterized by a 50-150 m nocturnal inversion of about a 1-4 K strength. A nocturnal jet is also observed just below the inversion. They note that during rain cases the inversion and jet are weaker than for dry cases due to cloudiness and vertical mixing. The depth of the downslope flow, however, was generally deeper than the dry cases due to evaporative cooling of the falling raindrops. They suggest that the onset of upslope flow may occur by three different mechanisms, progressing downward within the downslope layer due to shear instability, simultaneously at all levels when the layer becomes well mixed, and at the lower levels in contact with the slope and progressing upward. During the afternoon transition to downslope flow, the slope surface becomes cooler than the environment a couple hours before sunset with the downslope flow beginning 30-45 minutes later. During rain events, a much earlier downslope flow initiation was observed in the lowlands area most likely due to evaporative cooling of raindrops and the outflow of cool downdrafts from showers on the upper slopes.

Carbone et al. (1995) is in agreement with previous HaRP analyses in describing the downslope flow as primarily a thermally driven circulation. They compared the westerly downslope flow to a classic gravity current with a 1% density discontinuity across the flow convergence line. Similar to previous studies, Carbone's analysis underlines the importance of precipitation on the development of the downslope flow. Here, however, they suggest that evaporation is the primary cause of the downslope flow initiation on most days.

Feng and Chen (1996) presented a case study of downslope flow evolution on 10 August, 1990. This relatively dry case under normal trade-wind strength reflected the importance of the diurnal heating cycle in the development of downslope flow. They found that downslope flow was initiated on the upper slope by radiative cooling. At the coast, the windshift to downslope flow occurred as the drainage front arrived from the lowlands. As the cold pool at the coast deepened through the night, downslope flow was able to extend 15-17 km offshore before sunrise.

Wang and Chen (1996) is one of the first studies of the rainband evolution. Previous HaRP analyses have been concerned with upslope/downslope flow evolution, thermal forcing, and the effects of precipitation. In this case, they investigate the early morning rainbands using Doppler radar and aircraft data. They found that the rainband existed well before encountering the convergence zone between offshore flow and trade winds. Enhancement of the rainband was observed, however, as it encountered the downslope flow.

As revealed by previous studies, precipitation over windward sections of the island of Hawaii is not fully understood. Larson (1978) described much of the trade-wind rainfall in the summer months to be from sub-synoptic scale disturbances. Many other

6

investigators characterize windward precipitation by two regimes, afternoon orographically enhanced rainfall and nighttime showers from the rainbands moving onshore. Schroeder et al. (1977) and Takahashi (1977) found a nocturnal rainfall maximum at coastal stations. Chen and Feng (1995) observed that most nighttime rainfall began in situ from showers originally over the upper slopes during the late afternoon and early evening. They also highlighted the importance of large scale conditions in determining rainfall frequency. Modeling studies suggest that dynamic interaction with the island barrier is responsible for the timing and location of precipitation (Smolarkiewicz et al. 1988) indicating that precipitation is a result of island-scale forcing.

1.3 Scientific objectives

The primary objective of the research proposed here is to document the interaction between island-induced flows and trade-wind showers. I wish to investigate the influence of nocturnal katabatic winds on rainshowers in the opposing trade-wind flow. It is believed that focusing and enhancement occurs as the trade-wind showers meet the leading edge of the downslope flow. To show that this interaction is truly binary, the effects of these trade-wind showers on initiation and evolution of nocturnal downslope flow will be investigated.

I have chosen 7-8 August to perform a detailed case study to illustrate the interaction between island-induced flows and trade-wind showers. One of the reasons for selecting 7-8 August, is that it is the wettest 03-07 HST period during HaRP (Fig. 1.2). Analysis of the Doppler weather radar data suggests that almost all of the early morning rainfall is from offshore trade-wind showers drifting onshore. As these trade-wind

7

showers move toward the island, they interact with the island-induced circulations. These showers are enhanced by the convergence caused by interaction between downslope flow and incoming trade winds along the coast. Although some of these showers have band-like features, it appears that these are not "traditional" rainbands discussed in previous studies.

In addition to the rainfall studies, I will use the surface based PAM and tethersonde data to investigate the evolution of low-level airflow over land, particularly the effects of these showers on thermally driven nocturnal downslope flow. Some of the strongest upstream trade winds of the HaRP experiment are observed on 7-8 August. This provides a unique opportunity to study the downslope flow evolution under strong trade-wind forcing. Chen and Nash (1994) found that for strong trade-wind cases, the duration of nighttime downslope flow is shorter than weak trade-wind cases. I intend to intensively investigate the transition periods between upslope and downslope flow on 7-8 August to better understand the mechanics of how this transition occurs under strong trade-wind conditions.

CHAPTER TWO

DATA ANALYSIS

The data used in this thesis come primarily from sensors deployed during the HaRP experiment. These include PAM stations, tethersonde soundings, research aircraft flights, radar observations, a data from a boundary layer wind profiler. Other data sources include rawinsondes launched by the National Weather Service (NWS) at Hilo airport, synoptic charts, and satellite imagery from GOES (Geostationary Operational Environmental Satellite) and NOAA (National Oceanic and Atmospheric Administration) satellites. The period selected for this study is from 1500 HST on 7 August 1990 to 0900 HST on 8 August 1990 within the intensive observation period (IOP) for the experiment.

2.1 PAM data

A network of 50 PAM stations was deployed on the island (Fig. 2.1) to record surface parameters at 1-minute intervals. Pressure, temperature, wet-bulb temperature, u and v wind components, and rainfall were measured by the standard PAM station. The HaRP Data Catalog (1990) describes details on resolution and accuracy of the sensors used in the experiment. From the standard measurements, other derived quantities were calculated. Equivalent potential temperature is calculated by Bolton's formula (1980). Dry static energy, defined as,

$$s \equiv C_p T + gz \tag{2.1}$$

where C_p is the specific heat of air at constant pressure, T is temperature, g is the gravitational acceleration, and z is altitude. Moist static energy, defined as,

$$h \equiv C_p T + gz + Lq \tag{2.2}$$

which is the dry static energy plus the Lq moisture term where L is the latent heat of vaporization, and q is the specific humidity. Other variables calculated from the original PAM surface data include dew point, virtual temperature, and virtual potential temperature.

Many of the analyses presented in this study are timeseries of the original 1-minute data. In these cases a careful manual inspection was used to eliminate obvious errors and unreasonable data spikes. The surface wind fields are based on 15 minute averages after error checking and elimination of suspect data that is described in Chen and Nash (1994).

Stations 15 and 16 (Fig. 2.1) include additional radiation measurements. Variables measured include global solar incoming, downward infrared, solar diffuse, solar reflected, and net "all wavelength" radiation. The global solar incoming radiation was missing at station 16 due to an instrument problem, however, the net radiation values remained unaffected. The accuracy and resolution of the radiation instruments are contained in the HaRP Data Catalog (1990).

Some PAM stations were particularly problematic during HaRP. In addition to the radiation sensor problem at station 16, the tipping bucket rainguage at station 15 malfunctioned rendering all rainfall data for this site unusable. Station 5 suffered from poor wind exposure and no wind analyses incorporate this station.

2.2 Tethersonde data

Tethersonde operations were conducted at Kaumana Elementary School (Fig. 2.1) during 7-8 August 1990. The tethersonde instrument was manufactured by Atmospheric Instrument Research (AIR) and measured pressure, temperature, wet-bulb temperature, relative humidity, and wind speed and direction at about a 5-10 m resolution. Accuracy and resolution of the instrument package is contained in Wang (1995).

The tethersonde instrument had difficulty during periods of rain. Moisture values were particularly troublesome during rain periods due to sensor wetting. Immediately after rainy periods, temperature was usually unrealistically low as the previously wet temperature sensor was prone to evaporative cooling in drier conditions. The tethersonde log indicated that it took several minutes after the rain for the temperature sensor to produce reliable values. Based on these problems, tethersonde operations were usually terminated during rainshowers. No attempts have been made to correct the data other than removing obvious data spikes. Some of the analyses presented show evidence of contamination mentioned above and are used cautiously.

2.3 Hilo rawinsonde data

During the period covered by this study, rawinsondes were lunched from Hilo at 1400 HST, 2300 HST, 0200 HST, 0500 HST, and 0800 HST. These represent the supplemental sounding strategy during the intensive observing period. Ahnert (1990) lunched two instrument packages on the same balloon to measure the consistency of the sonde packages. The results indicate good agreement in the low levels with 95% of

temperature and humidity comparisons having a difference of only 0.5% and 2.5% respectively. The soundings for the 7-8 August 1990 case, however, were plagued by missing wind data in the near surface layer and were of limited value in monitoring low-level winds near Hilo. Temperature sensor wetting was a problem for the rawinsonde packages when passing through rain and clouds. Many of these soundings exhibited unrealistic superadiabatic lapse rates after reaching the base of the inversion. This is a common problem for Hawaiian soundings and occurs when the temperature sensor becomes wet passing through clouds and then cools by evaporation when it encounters the very dry air above the inversion. The sensor eventually dries and produces more accurate readings. I corrected for these superadiabatic lapse rates near the inversion base using the method formulated by Grindinger (1992).

2.4 Aircraft data

The National Center for Atmospheric Research (NCAR) Electra provided aircraft measurements during HaRP. Two flights were conducted for the period of interest, the first beginning at 2109 HST on 7 August 1990 and ending at 0144 HST on 8 August 1990, and the second from 0400-0735 HST on 8 August 1990. The HaRP Data Catalog (1990) describes the instruments and performance characteristics of the aircraft. These flights included an upstream sounding taken approximately 140 km from Hilo. The aircraft soundings were prone to the same sensor wetting problems observed with the Hilo soundings. These soundings also contained unrealistic superadiabatic lapse rates at the top of the moist layer. The same technique used for the Hilo soundings were applied to correct the aircraft soundings (Grindinger 1992).

12

Since some analyses in this study compare values from the upstream sounding with values from PAM stations at the same elevation, a comparison was made between the two instrument platforms to check for any biases. I compared temperature and wet bulb from the aircraft while on the ground shortly before takeoff and after landing with the values measured at the PAM station (station 9) located at the airport. One of the periods for comparison was discarded due to shower activity at the airport and the threat of contamination of moisture values. The comparison between the PAM station and aircraft yielded temperature and dew point values within a range of 0.5 ^{o}C of each other. No systematic bias was detected, so no correction was possible.

In addition to the upstream sounding, several low level (150-200 m) legs near the island were used to evaluate the evolution of near-surface winds. Data from final approach and takeoff were also used to monitor the low-level wind field near Hilo. In both cases, altitudes were measured by the Sperry radio altimeter due to contamination of the Stewart-Warner radar altimeter at low altitudes (HaRP Data Catalog 1990). The HaRP Data Catalog also reported potential Inertial Navigation System (INS) errors in turns and particularly climbing turns which affect the wind measurements.

2.5 Radar data

During HaRP, two C-band Doppler radars were operated at Paradise Park (CP-3) and Hilo Airport (CP-4). Characteristics of the radars are contained in the HaRP Data Catalog (1990). Most of the data used in this study are surveillance scans of reflectivity from CP-4 at beam elevations of 0.5^{o} for long range interrogation and 4.5^{o} as echoes neared the coastline. The beam elevation of 4.5^{o} was chosen to minimize ground signals

allowing uncontaminated viewing of radar echoes over the eastern side of the island. Range-height indicator (RHI) scans at azimuths directed eastward over the water were used from both CP-3 and CP-4 to investigate near-surface winds using reflectivity and radial velocity fields.

2.6 Profiler data

A NOAA 915 Mhz ultrahigh frequency boundary layer wind profiler was located at Paradise Park (station 8). Resolution and accuracy of the instrument are contained in Grindinger (1992). The profiler usually detected clear air echoes up to 4 km with a 104 m height resolution. Sampling intervals were every 12 minutes for reflectivity and every 30 minutes for wind profiles.

CHAPTER THREE

LARGE-SCALE CONDITIONS

The purpose of this chapter is to describe the synoptic and mesoscale weather conditions on 7-8 August 1990. I will use synoptic charts, satellite imagery, and soundings to provide a detailed overview of the important large-scale features. These datasets will also provide limited analysis of smaller scale features that also have an effect on the island weather conditions for this case study.

3.1 Synoptic analysis

The large-scale picture on 7-8 August 1990 is best described by NWS surface and upper air analyses. Fig. 3.1 shows the surface analysis at 1400 HST on 7 August 1990. The surface pattern is dominated by two high pressure centers north of the island chain with a ridge axis between them. Weak ridging is evident west of the island along 160° W. East of the islands however, the surface pressure gradient appears to be tightening, probably influenced by the tropical storm located far south of the islands. Aside from the tropical storm and its effects on the pressure field, the surface pattern is typical for August (Chen and Feng 1995). The upper air analysis (Fig. 3.2) indicates a broad high pressure center south of the islands and a ridge extending northward through the western island chain. A closed low center and positive tilt trough can be seen west of the islands near the dateline. A 25 m s^{-1} jet streak is observed extending from exit region of the low center and curving anticyclonically around the ridge that exists over the islands.

Many of the synoptic-scale features evident in the surface and upper-level analyses are reflected in the visible GOES satellite image at approximately the same time (Fig. 3.3). Located far east of the islands is a patch of closed cell stratocumulus reflecting the influence of the surface high pressure in that area. At the far west side of the image, layered middle and upper cloudiness exist in the presence of the upper low shown in the 250-hPa analysis (Fig. 3.2). Closer to the islands, upper level cloudiness can be seen coming from the south likely associated with the tropical storm. Upstream of the island chain a disturbed area of trade-wind cloudiness can be seen about 300 km east of Hawaii. This will be described in more detail in the next section. Otherwise, trade winds appear to be occurring with a well defined cloud-free wake in the lee of the island chain, especially in the northern sections. In the lee of the southern part of the chain, many low-level clouds exist suggesting a complicated lee side circulation structure in the lee of the big island.

The Hilo rawinsonde (Fig. 3.3) indicates trade winds with a peak of about 7 m s^{-1}. Although no true temperature inversion exists until the 2.6 km level, an isothermal profile in temperature and the clear drying in dew point at 1.8 km representing the top of the moist layer suggest the trade-wind inversion is at this level. One must be cautious, however, in the reliability of the sounding taken at Hilo as representative of the large-scale environment. Many investigators (e.g. Leopold 1949, Lavoie 1967) have described the variability of the trade wind inversion over the island. Garrett (1980) showed how local circulation systems can affect the inversion height, resulting in a lower height during the day in the presence of broad descending motion of the sea breeze return flow over water. A lower daytime inversion height was also found by Grindinger (1992) in her profiler inversion study. In addition, the wind speeds in the Hilo sounding are likely decelerated as trade-winds approach the island as suggest by Smolarkiewicz et al. (1988). Fortunately, the HaRP

16

project featured upstream soundings by the NCAR Electra usually about 140 km east of Hilo in an attempt to eliminate the effects of the island itself on the sounding. Fig. 3.5a is an upstream sounding at 2100 HST on 7 August 1990. The differences between this sounding and the one from Hilo (Fig. 3.4) are clear. First, the trade winds are much stronger with peak values of 11 m s^{-1} which represent some of the strongest trade winds observed in the HaRP project. Average HaRP values were closer to 7 m s^{-1} as shown in Chen and Nash (1994) their Fig. 3. The other key difference is the height of the trade-wind inversion which is about 2.8 km in the upstream sounding. The next section will explore more details about this difference.

3.2 Mesoscale features

As mentioned in the previous section, an area of disturbed trade-wind cumuli is present east of the island (Fig. 3.3). The synoptic-scale analyses provide no explanation for its existence. The forcing for this area must lie on a smaller scale, most likely a mesoscale phenomenon. It is suspected that this area has a profound influence on the island weather conditions for 7-8 August 1990. A sequence of GOES satellite images (not shown) indicated that this area is moving towards the island embedded within the trade-wind flow. A NOAA image at 0208 HST (Fig. 3.6) shows a better view of the area as it nears the coast. It will be shown in later chapters that this area appears to be source of the observed precipitation during the 7-8 August period.

The disturbed area of cumuli appears to have affected the upstream aircraft soundings. Fig. 3.5b shows a satellite image from 2130 HST that indicates the disturbance has moved closer to the islands. From this satellite image it appears that the upstream

17

sounding was taken within this disturbed area. The sounding (Fig. 3.5a) shows the trade-wind inversion at 2.8 km with a rather moist layer below. Several hours later at 0400 HST another upstream sounding (Fig. 3.7a) shows a lower inversion height of about 1.6 km and a generally drier moist layer then at 2100 HST (Fig. 3.5a). This sounding appears to have been taken in the clear area behind the disturbance as seen in the GOES satellite image at 0430 HST (Fig. 3.7b). It is speculated that the disturbed area and its attendant convection has raised to inversion locally similar to findings by Grindinger (1992) in her profiler studies where she noticed a higher inversion around rainshowers. In addition, the clear area behind the disturbance may be a result of subsidence, thereby lowering the inversion height. Although there are changes in the moisture and inversion structure, the wind profiles are very similar with strong trade winds of 11 m s^{-1}.

In summary, the large scale conditions for 7-8 August 1990 are dominated by strong trade winds with a mesoscale disturbed area superimposed within the trade-wind flow. Aside from the apparent tightening of the surface pressure gradient, the effects of the tropical storm to the south are an increase in upper level clouds that reach and cover the island by about midnight (not shown).

18

CHAPTER FOUR

EVOLUTION OF DOWNSLOPE FLOW

The purpose of this chapter is to perform a detailed analysis of the initiation and evolution of downslope flow on the evening of 7-8 August 1990. The primary dataset used for this analysis is the data collected by PAM stations on the windward side of the island. These data are supplemented, where available, with NWS soundings taken at Hilo Airport (PAM station 9), tethersonde soundings collected at Kaumana Elementary School (near PAM station 15), Doppler radar observations from CP-3 at Hilo Airport and CP-4 at Paradise Park (PAM station 8), profiler data from Paradise Park, and data collected from the two NCAR Electra flights that occurred that evening.

Two reasons make study of downslope flow initiation and evolution on the evening of 7-8 August particularly interesting. First, as indicated in Chapter 3, trade winds measured upstream are among the strongest observed during the HaRP experiment. Winds from the aircraft sounding at 2100 HST indicate trade-wind strength of 11 m s^{-1} (Fig. 3.5). I feel it is important to document the evolution of downslope flow in the presence of such strong trade winds. Observing the way downslope flow evolves under such conditions may help our understanding of the diurnally oscillating upslope/downslope regime on the windward side of the island. In addition to very strong trade winds, the evening of August 7-8 receives the highest early morning (0300-0700 HST) precipitation accumulation of the HaRP experiment (Fig. 1.2). It is clear from previous studies (Chen and Wang 1994, Carbone et al. 1995, and Chen and Wang 1995) that precipitation intensity and frequency play an important role on the evolution of downslope flow. I wish to

19

investigate how the relatively large rainfall amounts observed on the evening and early morning of 7-8 August affect the initiation and evolution of downslope flow.

4.1 Afternoon upslope flow

The analysis of downslope flow evolution on 7-8 August 1990 will first begin with a brief discussion of the preceding conditions on the afternoon of 7 August. Fig. 4.1 shows conditions at 1500 HST with upslope flow occurring over all of windward Hawaii. Peak wind speeds at this time are 4 m s^{-1} observed at several stations (station 7, station 6, and station 11), a considerable decrease from the upstream sounding that measured trade winds of 11 m s^{-1}. In addition to the deceleration, wind directions along the coast suggest flow is being deflected around the island as simulated by Smolarkiewicz et al. (1988), Rasmussen et al. (1989), and Rasmussen and Smolarkiewicz (1993). Fig. 4.1 also indicates the virtual temperature difference at 1500 HST between the PAM locations and the upstream sounding at the same elevation. Not surprisingly, virtual temperature over the land surface is warmer than the upstream ocean surface reinforcing previous studies (Chen and Wang, 1994) that suggest the importance of thermal contrast in development of upslope flow. A minimum of virtual temperature difference exists around station 15, 16, and 10. These stations are at 405, 1128, and 506 meters above sea level respectively and lie at a location dominated by orographic cloudiness. Fig. 4.2 shows a NOAA satellite image at 1335 HST that shows clouds covering most of the island except over the two volcano peaks. It is suspected that this cloudiness serves to limit incoming solar radiation and result in lower surface temperatures than more cloud-free locations.

4.2 Evening transition

High resolution (1 min) PAM data will be used to study the transition from upslope to downslope flow over the windward side of the island. Fig. 4.3 indicates downslope flow first occurs on the upper slopes and then gradually progresses down to the coast. Compared to HaRP mean values (Chen and Nash 1994), the 7-8 August case features much later occurrence of downslope flow over the windward lowlands and coastal areas. Some locations (station 13, 9, and 8) undergo transition from upslope to downslope flow more than two hours later than the HaRP mean. Clearly this is due the atypically strong trade winds observed on 7-8 August 1990. Cape Kumukahi (station 7) never experiences a downslope wind direction, remaining well exposed to trade-wind flow the entire evening.

4.2.1 Downslope flow initiation on upper slopes

To investigate downslope flow initiation on the upper slopes, an analysis of radiation and thermodynamic data from station 16 (1128 m) will be conducted. During the afternoon hours net radiation values are highly variable, this is likely due to the fluctuation of coverage by orographic cloud. Variation in cloudiness affects both direct beam isolation and downward longwave radiation, thus producing large amplitude changes in net radiation over very short time intervals (Oke, 1987). Fig. 4.4a shows some phase agreement between the IR down and net radiation values indicating the influence of the orographic cloudiness on the surface radiation balance. It is important to also note that temperature (Fig. 4.4b) shows good correlation with net radiation. Clearly, surface temperature is responsive to surface radiation flux. Net radiation begins to decrease shortly before 1700

21

HST and becomes negative at 1730 HST, a similar drop also occurs in temperature at this time. At the same time, IR down values drop suggesting a partial clearing of the orographic cloud. Shortly afterward, however, a sharp increase in IR down is indicated. It appears that orographic cloud is becoming reestablished over the station. Shortly after 1730 HST temperature begins to climb again in response to an increase in net radiation until approximately 1800 HST.

Wind data (Fig. 4.4e) indicate sustained downslope flow first starts at about 1915 HST. This is within one hour of virtual temperature reversal between the station and the upstream sounding at the same elevation (Fig. 4.4e) as mentioned by Chen and Wang (1994). At the time of downslope flow transition, a steady decrease in dry static energy and specific humidity (Fig. 4.4d) combine to produce a fall in moist static energy (Fig. 4.4c). The behavior of the thermodynamic parameters suggest that radiative forcing is responsible for the observed cooling and subsequent initiation of downslope flow. There is no evidence that evaporation plays any part in the downslope flow transition on the upper slopes (Carbone et al., 1995). If evaporation was occurring, a drop in dry static energy would accompany and approximately offset the increase in specific humidity, producing little change in moist static energy. This, however, is not observed. Rainfall data for the afternoon of 7 August (not shown) indicates only 0.25 mm of rainfall occurs over the entire windward side of the island between 1400 HST and 1900 HST. This rainfall occurs at station 10 at an elevation that is more than 500 meters below station 16.

4.2.2 Downslope flow arrival over windward lowlands

Data from station 15 will be used to investigate downslope flow initiation over the windward lowland. Radiation data (Fig 4.5a) are similar to station 16 with highly variable

22

values of net radiation during the early afternoon. Temperature (Fig 4.5b) appears to fall from about 1600 HST to 1700 HST in agreement with a similar decrease in net radiation (Fig. 4.5a), although net radiation remains positive. This is due to strong sensible heat fluxes from the surface. Shortly before 1700 HST an increase in net radiation, IR down, temperature, and dew point is observed. This appears to be related to an increase in orographic cloud coverage. Net radiation begins to drop sharply after 1715 HST with temperature following similarly. Net radiation first becomes negative at 1745 HST, but only briefly as continued variability in IR down results in another increase in net radiation. Finally at 1845 HST net radiation becomes negative for the rest of the evening. At the same time temperature and dew point (Fig 4.5b) decrease as a sustained downslope wind component (Fig 4.5b) is first observed at 1945 HST. Similar to the upper slopes, it appears that evaporation plays no role in development of downslope flow at station 15. Downward trends are observed in moist static energy (Fig. 4.5c), dry static energy (Fig. 4.5d), and specific humidity (Fig. 4.5d). Like the upper slopes, wind reversal at station 15 occurs within one hour after the virtual temperature difference between the PAM site (Fig 4.5c) and upstream becomes negative.

4.2.3 Development of drainage front over lowlands

As downslope flow becomes well developed over the upper slopes and windward lowland between 1900 HST and 2100 HST, coastal sections still experience warm trade-wind flow. Continued cooling is observed at station 15 (Fig 4.4b) and 16 (Fig 4.5b) after downslope flow starts. At station 16, temperature and dew point (Fig. 4.4b) steadily decrease until about 2015 HST when a sharp decrease in both values is indicated. At the same time a significant decrease is observed in IR down indicating a clearing of the

orographic cloud formerly over the station. Afterwards, dew point drops dramatically as downslope component reaches 4 m s^{-1} (Fig 4.4c). The clearing of orographic cloud as downslope flow becomes well developed has been noted by Chen and Wang (1994) and Chen and Wang (1995).

At 2100 HST a pool of cold air begins to "pile up" over the windward lowland west of Hilo. Fig. 4.6a shows an elongated area of minimum virtual potential temperature (theta v) at the leading edge of the downslope flow. This marks the location of the drainage front, or the separation of the cool, dry downslope flow from the warm, moist trade wind flow. This situation is very similar to the 10 August case (Feng and Chen, 1996) where the pool of cold drainage flow lies over the lowlands and is held up from moving toward the coast by trade-wind flow. In the 10 August case, the gradient of theta v between the lowlands and the coast provides the forcing for the drainage front to move toward the coast. It should be noted, however, the 10 August case occurs under normal to weak trade winds compared to the HaRP mean. In the 7-8 August case, the uncharacteristically strong upstream trade winds of 11 m s^{-1} do not allow the drainage front to move to the coast. Here, a different mechanism is responsible for allowing downslope flow to reach the coast. That mechanism will be discussed in the next section.

4.2.4 The effect of trade-wind showers on drainage front location

As mentioned above, downslope flow over the upper slopes and windward lowlands becomes well developed by 2100 HST with the drainage front located just west of Hilo (Fig. 4.6a). By 2130 HST IR down radiation at station 16 (Fig. 4.4a) jumps from 315 W m^{-2} to 375 W m^{-2}. This seems to suggest a return of cloudiness over station 16, which contributes to an increase in temperature and dew point (Fig. 4.4b). It is interesting

24

to note that the minimum temperature for the evening at station 16 occurs at 2145 HST before the increase in cloudiness. This is quite different from typical HaRP conditions when minimum temperatures are usually observed near sunrise (Chen and Nash, 1994).

Interesting changes in the surface theta v field occur between 2100 and 2200 HST over the coast and lowland area. Fig. 4.6b indicates that the well defined cold pool over the lowland area west of Hilo has become disorganized. In addition, the drainage front has moved westward back up the slope. Station 13, 44, and 4 have undergone a wind shift from downslope flow back to a trade-wind direction. There is significant cooling along the coast and warming observed at inland stations, including those that have undergone a shift back to easterly winds (Fig. 4.7a). Significant rainfall accumulations are observed over the coast and lowland areas between 2100 and 2200 HST (Fig. 4.7b). These showers are carried over the coast by the trade wind flow layer, and will be discussed in more detail in chapter 5. The cooling/warming pattern and retreat in the drainage front between 2100-2200 HST appears to be related to rainshowers.

I will first investigate the observed cooling along the coast. Fig. 4.7a shows cooling over the entire coastal area between 2100 HST and 2200 HST, where, in all cases, at least 0.25 mm of rainfall has occurred (Fig. 4.7b). The time series data for station 8 show a large temperature drop (Fig. 4.8a) occurs at about 2130 HST, while from 2130-2145 HST a steady increase in dew point (Fig. 4.8a) is observed. A similar signal is observed in the dry static energy and specific humidity values (Fig. 4.8c). A sharp trade-wind component of near 6 m s^{-1} is also observed at the same time as the temperature drop (Fig. 4.8d). Some rainfall is also observed between 2130-2145 HST (Fig. 4.8b). The magnitude of the temperature drop and the strong easterly wind component suggest the possibility that a gust front has passed the station. At the very least, the thermodynamic

25

variables confirm that evaporation is taking place as rainshowers occur under trade-wind conditions.

I will next look at the warming occurring after rainshowers (Fig. 4.7a) and the destruction of downslope flow there (Fig. 4.6b). At station 15, a jump is noticed in temperature and dew point (Fig. 4.5b) at 2215 HST. A similar ramp-up in dry static energy and specific humidity (Fig. 4.5d) is also observed. At approximately the same time as the temperature and moisture increase, a sharp return to easterly wind component (Fig. 4.5e) is observed. This is quite interesting, as downslope flow had been occurring since 1930 HST. Unfortunately, rainfall data is missing at station 15, however, detailed observations by tethersonde operators are available at nearby Kaumana Elementary School. Those observations are included in Fig. 4.5c. It appears that the jump in temperature and moisture and the switch from downslope to easterly winds occurs as moderate to heavy rainshowers are reported. It seems that the vertical mixing associated with rainshowers is transporting potentially warmer air from aloft down into the near-surface downslope flow layer. The observed increase in moist static energy (Fig. 4.5c) that occurs very near the time that moderate to heavy rainshowers are reported by the tethersonde crew show evidence of this phenomenon. It is believed that the vertical mixing also transports easterly momentum from the trade-wind layer into the downslope flow layer causing a temporary destruction of downslope flow and a return to easterly winds.

Evidence of vertical momentum transport can be seen in the tethersonde data at Kaumana Elementary School. Although the thermal profiles (Fig. 4.9a and b) are contaminated by rainshowers, the wind data (Fig. 4.9c) shows the effects of the vertical mixing. A sudden reversal from westerly downslope flow to easterly trade-wind flow can be seen within the 975-955 hPa layer from 2102 HST to 2212 HST. As seen from Fig.

26

4.5b, rainshowers of moderate and then heavy intensity were reported during this time by the tethersonde operators. The sharp return to easterly winds at 2212 HST is followed by a resurgence in downslope flow at 2302 HST with decreasing temperature and dew point. Furthermore, evaporation could be occurring aloft after the rainshowers that enhance the return to downslope flow. It is noted that at 2302 HST downslope winds of about 6 m s^{-1} are evident and represent the strongest downslope flow observed at the tethersonde site. It is interesting that although the rainshowers destroyed the downslope flow for a short period, afterwards, stronger downslope winds are observed, likely due to evaporation in the near-surface layer.

4.2.5 Downslope flow arrival at the coast

So far we have observed downslope flow transition on the upper slopes and over the windward lowland. Thermal contrast between the land surface and the upstream ocean surface appears to be the physical process responsible for the transition. It also appears that the cooling on the slope surface occurs due to radiative heat loss and not evaporative cooling as suggest by Carbone et al. (1995).

Downslope flow arrival at the coast occurs after rainshowers have occurred there. It appears, unlike the initiation of downslope flow on the upper slopes and lowlands, evaporation has provided some of the observed cooling prior to downslope flow arrival. The cooling, in this case, should not be mistaken for cold pool arrival at the coast signifying development of downslope flow as in the 10 August case (Feng and Chen, 1996). It is clear that cooling along coastal areas shown in Fig. 4.7a occurs prior to downslope flow arrival (Fig. 4.6b). Fig. 4.8 shows downslope flow transition at station 8 in some detail. At this coastal station, the sharp drop in temperature (Fig. 4.8a) and

27

increase in trade-wind strength (Fig. 4.8d) has already been discussed. Shortly after the evaporative cooling, downslope flow is first observed at station 8 at 2215 HST.

By 2300 HST downslope winds are observed at the coast with the exception of Cape Kumukahi (station 7) where trade-winds prevail the entire evening. Fig. 4.10 indicates that the cold pool is now located over the coastal area near Hilo, thus completing the seaward progression of downslope flow over the windward side of the island.

4.2.6 Summary of downslope flow transition

The initiation of downslope flow over windward sections of the island can be attributed to two different processes. It is clear that initiation on the upper slopes and over windward low lands is triggered by radiative cooling of the land surface. In contrast to studies by Carbone et al. (1995), the lack of rainfall during the later afternoon to early evening on August 7 1990 make it highly unlikely that the observed cooling prior to downslope flow onset can be attributed to evaporation of precipitation. In addition, the thermodynamic variables at these locations are consistent with radiative cooling. The data for August 7 1990 suggests that downslope winds over the upper slopes and lowlands are observed within one hour of the sign change of the difference in virtual temperature between the PAM station and at the same altitude upstream. This is similar to studies by Chen and Wang (1994).

While the role of radiation forcing is quite clear on the upper slopes and lowland areas, downslope flow transition over coastal areas appears to be from a different process. Here the role of trade-wind showers and the precipitation they bring play an important part. The fact that downslope winds are only observed at the coast after significant precipitation has fallen and the presence of evaporative cooled cold air at the surface (Fig. 4.8a) before

28

the flow reversal (Fig. 4.8d) suggest that rain evaporation cooling is an important factor for flow reversal at the coast.

4.3 Evolution of downslope flow after midnight

In this section I will investigate the evolution of downslope flow from about midnight on 8 August 1990 until the transition to upslope flow later in the morning. This period offers a unique opportunity to study the effects of strong trade winds and frequent trade-wind showers on the downslope flow. I intend to show that mixing associated with showers under the influence of stronger than normal trade winds disrupt the downslope flow and cause an oscillation of the drainage front from off the coast to inland regions.

4.3.1 Near-midnight conditions

As seen in Fig. 4.10, by 2300 HST downslope flow is observed over all of the windward side except at Cape Kumakahi (station 7). At 2300 HST, the drainage front is somewhere offshore based on the virtual potential temperature distribution (Fig. 4.10). Some evidence of offshore flow can be seen from data from the low-level Electra flight leg near the coast (Fig. 4.11). The flight leg that runs parallel to the coast was conducted from about 2228-2300 HST, with the winds sampled between 150-200 m. Offshore winds can be seen north of Hilo Bay and just offshore from Hilo airport. Further to the south near Paradise Park, however, trade winds are observed. The small extent of offshore flow at this time is due to the abnormally strong trade winds. Just as the trade winds delayed the initiation of downslope flow at the coast as mentioned in the last section, they also prevent downslope flow from moving a large distance offshore.

The strongest downslope winds are observed during the near midnight hours. This can best be seen in the tethersonde wind profiles (Fig. 4.9c). Downslope winds of over 6 m s^{-1} occur near 965 hPa at 2302 HST and 5.5 m s^{-1} at 0135 HST. By 0245 HST, however, only a few winds of 4 m s^{-1} are observed. This is a departure from HaRP mean conditions. Usually, the best developed downslope flow occurs near sunrise when most thermodynamic variables such as temperature reach their minimum value for the morning. The difference in the 8 August case is the effects of the early morning rainfall. Data from station 15 show this phenomena (Fig. 4.5). The diurnal minimum in temperature and dew point (Fig. 4.5b) occurs near midnight, not near sunrise as in the HaRP mean. Downslope wind components at this time (Fig. 4.5e) are near 4 m s^{-1} which are the peak values for station 15. In the hours following midnight, a steady increase is observed in temperature and dew point (Fig. 4.12b). The reason for the increase is linked to vertical mixing due to rainshowers and abundant cloudiness that limits outgoing longwave radiation and hence retard surface cooling. As dew point and temperature increase after midnight, the downslope wind component falls from about 4 m s^{-1} from 2300-0000 HST (Fig. 4.5e) to about 2 m s^{-1} from 0100-0300 HST (Fig. 4.12e). In summary, the strongest downslope winds are observed when thermodynamic values are at a minimum, which for the 7-8 August case, occur near midnight.

4.3.2 Drainage front oscillation

After several hours of sustained downslope flow over the windward coast, changes begin to occur around 0400 HST. Fig. 4.13a shows downslope flow extending to the coast at 0300 HST. The virtual potential temperature distribution is similar to that observed at 2300 HST (Fig. 4.11) when downslope flow first reached the coast. The winds and theta v

30

distribution indicate that the drainage front is offshore, with the only onshore trade winds located at Cape Kumakahi. An RHI scan from CP-4 at Hilo airport at 0258 HST shows downslope flow extending to about 6 km offshore. The radial velocity data (Fig. 4.14b) shows a gravity head structure at the leading edge of the downslope flow similar to Carbone et al. (1995). Based on target point inspection of the radial velocity data, wind speeds with the head are near 1 m s^{-1} or less, while offshore components of 3-4 m s^{-1} exist between 3-4 km offshore. An RHI scan about 30 minutes later indicate that the downslope flow appears to be retreating. At 0328 HST (Fig. 4.15) the downslope flow has become poorly organized and extends only about 3 km offshore. Careful inspection of the low-level radial velocity (Fig. 4.15b) at 4-6 km reveals that strong trade-wind component winds have replaced the gravity current head structure that existed at 0258 HST (Fig. 4.14b). Target inspection in this area indicated on-shore components of over 10 m s^{-1}. There is evidence that the downslope flow is retreating and being replaced by easterly winds. Over the island, by 0400 HST (Fig 4.13b) trade winds are observed inland for the first time since downslope transition over the lowlands. Easterly winds are observed at stations, 9, 4, 44, and 8. The significant retreat inland of the drainage front can be seen in the theta v field in Fig. 4.15b. At 0400 HST, the minimum in theta v is now located much further inland with its axis along a line described by station 13, 44, and 4. This indicates there has been a disruption in the cold pool and the drainage front. This return to easterly winds is very similar to the backward oscillation of the drainage front at 2200 HST (Fig. 4.6).

Stations that undergo a oscillation from downslope flow to easterly winds experience a warming in theta v (Fig. 4.16a). Stations 9, 13, 4, 44, and 8 all experience an increase in theta v between 0300-0400 HST, with the maximum increase of 1.89 K at station 8. During the same time, all of these stations have experienced rainfall (Fig. 4.16b)

31

as much as 3 mm at station 8 and 13. The time series data at station 8 (Fig. 4.17) shows the return to easterly winds in detail. The temperature and dew point trace (Fig. 4.17a) show an increase in both parameters at 0330 HST, at nearly the same time as over 1 mm of rainfall occurs in only 1 minute. Also at 0330 HST, a sharp shift from downslope flow component to an easterly wind component occurs (Fig. 4.17d). This shift is very rapid and involves a 3 m s^{-1} downslope component to a 4 m s^{-1} easterly wind component in only a few minutes time. It appears that vertical mixing from rainshowers is again occurring. This is similar to what was observed at station 15 around 2200 HST (Fig. 4.6). The presence of vertical mixing is evidenced by the large jump in moist static energy at 0330 HST (Fig. 4.17b). In the presence of evaporation, the vertical mixing is bringing potentially warmer air from the trade-wind layer into the shallow near-surface downslope flow layer. This produced the warming at the surface as seen in the temperature (Fig. 4.17a) and dry static energy (Fig. 4.17c) time series. In addition, the mixing is also transporting easterly momentum from the trade-wind layer into the near-surface layer thereby destroying the shallow downslope flow and replacing it with easterly winds (Fig. 4.14b and 4.15b)

The destruction of downslope flow and its replacement by easterly winds can be seen in the boundary layer profiler data (Fig. 4.18) also at Paradise Park (station 8). The low-level wind data from the profiler (Fig. 4.18a) shows weak downslope winds below 400 m from 0000-0300 HST. Shortly after 0300 HST, however, easterly winds of almost double the strength of the downslope flow are occurring throughout the near-surface layer. At the same time, the reflectivity data (Fig. 4.18b) shows the classic rainshower signature of high reflectivity areas surrounded by lower values (Grindinger 1992). Clearly, the rainshower, through vertical mixing has destroyed the downslope flow and has allowed

32

easterly winds to mix down to the surface. It is interesting to note that easterly winds at the surface after 0300 HST seem to be the same direction and speed as the winds above the downslope flow layer during the previous hours. It is suggested that these winds have lowered to the surface in the presence of the rainshowers by vertical momentum transport.

Evidence of vertical mixing is also contained in the three-hourly Hilo soundings (Fig. 4.19). At 0200 HST, a temperature inversion exists from the surface to 120 meters with the strength exceeding 1 K. As reflected in the wind profile (Fig. 4.19c), downslope flow exists with the surface to 400 meter layer with trade winds above. It should be noted that like previous studies (Feng and Chen 1996), downslope flow extends above the nocturnal inversion. A few hours later at 0500 HST, the inversion has weakened to less than 0.5 K and extends only to 80 m. Almost 1K of warming is observed in the near-surface layer up to 100 m from 0200 HST to 0500 HST. Above 100 m, a cooling of about 1 K occurs throughout the 100-500 m layer. This appears to be a signal of vertical mixing due to rainshowers. The PAM station near Hilo Airport (station 9) reports 1.27 mm of rainfall between 0200 HST to 0500 HST (not shown). The vertical mixing associated with the rainshowers cause potentially warmer air aloft to mix with the cold surface downslope air resulting in the destruction or weakening of the nocturnal inversion. Aloft, evaporation is producing cooling above the inversion level. This can also be seen in the equivalent potential temperature profiles (Fig. 4.19b). A significant increase in theta e in the lowest levels from 0200 HST to 0500 HST can be seen. The increase can only come from above where higher values of theta e exist. Due to lack of low-level wind data, the effects of mixing on downslope winds can not be evaluated.

After the period of trade winds at station 8, a resurgence of downslope flow is observed. This occurs after another area of rainshowers moves over the station (Fig.

33

4.17b). Shortly before the rainfall around 0500 HST, an increase in dew point (Fig. 4.17a) and specific humidity (Fig. 4.17d) are occurring as temperature decreases suggesting the possible influence of evaporation. Shortly after these trends in temperature and dew point, a return to downslope winds is observed at 0545 HST. Interestingly, moist static energy, a conserved property for changes of state, is nearly constant from 0515 HST to 0630 HST (Fig. 4.17b). It is possible that the precipitation occurring under trade-wind flow is being evaporated and providing the cooling to allow downslope flow to return. This is similar to what was observed during the 2100-2200 HST period in which, under trade-wind flow at the coast, evaporative cooling of the precipitation allowed downslope flow to reach coastal areas.

As downslope flow is again returning to coastal areas, the drainage front again appears to be pushed offshore. Horizontal distribution of theta v at 0600 HST (Fig. 4.20) is similar to Fig. 4.10 when downslope flow first extended to the coast at 2300 HST. The area of minimum theta v is located at the coast indicating the location of the cold pool and the leading edge of the drainage front, which appears to be offshore. Unfortunately, RHI scans were discontinued by this time at both radar sites, making determination of offshore extent of the downslope flow difficult. However, a low-level flight leg from the second aircraft mission was flown along the coastline from 0500-0545 HST (Fig. 4.21). No evidence of downslope flow exists from the aircraft data. The lack of significant offshore extent at this time is not typical during HaRP. Feng and Chen (1996) found a significant offshore flow to about 15-20 km for the 10 August 1990 case, which occurred under normal trade winds and relatively dry conditions.

4.3.3 Summary

A complete picture of the evolution of downslope flow over windward parts of the island is now revealed. For the second time, a retreat in the drainage front is observed as a band of showers moves over the island. This retreat is typified by westerly downslope flow being replaced immediately by easterly winds in the presence of vertical mixing induced by the showers. This vertical mixing transports strong trade-wind momentum from aloft into the downslope flow layer thereby destroying it and bring easterly winds in its wake. This process of mixing potentially warmer air from aloft with the cooler air near the surface almost always results in a temperature increase and certainly an increase in moist static energy at the surface. This signal is well represented over lowland and coastal locations during the band of showers between 0300-0400 HST. Combining observations from the 2100-2200 HST rain period and the 0300-0400 HST period, the effects of rainfall on surface parameters during this case can be summarized by the following. Showers that occur under trade-winds (e.g. along the coast during the first rain period) tend to produce surface cooling likely due to evaporation. This was observed when downslope flow first reached the coast after the first rain period from 2100-2200 HST, over Cape Kumakahi during the second rain period from 0300-0400 HST, and at the coast again after 0500 HST. However, if showers fall as downslope flow is occurring underneath strong trade winds, vertical mixing brings easterly momentum aloft down to the surface and results in a wind shift and an increase in surface temperature and moist static energy.

4.4 Upslope flow initiation

The transition to upslope flow on the morning of 8 August 1990 occurs in a much different manner than the downslope flow transition. Overall, upslope flow occurs earlier than HaRP mean conditions. Almost the entire coastal and upper slope areas experience upslope flow between 0700 HST and 0800 HST (Fig. 4.22). For coastal areas, this is almost two hours earlier than the HaRP mean (Wang, 1995). Even more peculiar, previous studies (Chen and Wang, 1994) have shown that wet mornings experience even a later upslope flow transition than dry mornings. The 8 August case is clearly an exception. From Fig. 4.22, upslope flow begins on the upper slopes and coastal areas at nearly the same time. Similar to downslope transition, previous studies (Chen and Wang, 1994) have linked upslope flow with the reversal of virtual temperature difference between land surface and at the same altitude upstream. This does not hold on 8 August, however as shown by the high resolution PAM data at station 8 (Fig. 4.17). Zonal wind component (Fig. 4.17d) shows a transition to upslope flow near 0645 HST, while the virtual temperature difference is still negative. In fact, the virtual temperature reversal does not occur until 0730 HST.

The reason for early upslope flow transition on 8 August is related to the strength of the trade winds and onset of shear instability. This was first suggested as a possible factor by Wang and Chen (1995). The tethersonde wind data from Kaumana Elementary School (Fig. 4.23c) show at 0534 HST downslope flow extending to 965 hPa, above that, easterly trade winds are observed. Less than one hour later at 0718 HST, the downslope flow layer lowers to near 970 hPa with trade winds above. It appears that trade winds are lowering down to the surface from above. This is likely due to shear instability brought

36

about by strong trade winds that overcome the relatively weak vertical thermal gradients. The winds observed from the Hilo sounding at 0500 HST (Fig 4.19c) are nearly 9 m s^{-1} well above the HaRP average conditions. The thermal profiles from the tethersonde site indicate a dissipation of the normal nocturnal inversion as early as 0534 HST (Fig. 4.23a). This increases the chances of shear instability, especially considering the strength of the easterly winds in the trade-wind layer. It would be desirable to compute the Richardson number for the wind and thermal profiles from the tethersonde data (Fig. 4.23), however, the unreliability of the temperature data and the lack of adequate measurements of winds in both the trade-wind and downslope flow layer prevented meaningful computations.

CHAPTER FIVE

EVOLUTION OF TRADE-WIND SHOWERS

In the this chapter, I will study the trade-wind showers that occurred on 7-8 August 1990. Specifically, the effects of the interaction between downslope flow and trade-wind showers along the drainage front will be investigated. Radar reflectivity data from CP-4 at Hilo airport will be the primary tool for monitoring the evolution of trade-wind showers.

In chapter 3, satellite imagery (Fig. 3.3, 3.5b, 3.6, and 3.7b) revealed the existence of a disturbed area of trade-wind cumuli upstream of Hawaii. These images clearly showed that this area was moving towards to island in the trade-wind flow. Fig. 5.1 shows the total rainfall over windward sections of the island for the 1900 HST to 0700 HST period for 7-8 August 1990. Through the use of radar data, it will be shown that most of this rainfall is from trade-wind showers that drift over the island. It will also be shown that downslope flow and the drainage front enhance and focus the showers over coastal and lowland areas.

Two periods will be analyzed in this chapter. These periods represent the two best developed areas of rainshowers that drift over the island and show evidence of enhancement. The first is from 2100-2300 HST, and is the first significant rainfall for the evening. The second is from 0300-0500 HST where a well developed band of showers moves over the island from offshore. Both of these periods correlate well with the disturbed area of trade-wind cumuli that drifts toward the island (Fig. 3.3), with the largest, most developed area, coming ashore around 0300-0400 HST (Fig. 3.6). For continuity, these are the same shower periods that were investigated in the previous chapter. Whereas in the last chapter the effects of this rainfall on downslope flow was analyzed, here, the

38

effects of the interaction between downslope flow and trade winds along the drainage front on the band of showers themselves will be studied.

It should be noted, that the term "rainband" will be used frequently to describe the areas of showers during the two periods. In this case, the term is used simply to describe scattered trade-wind showers that take on a "bandlike" structure as they pass over the island. The reader is cautioned in applying this interpretation to other studies of the early morning rainbands (Wang and Chen 1996).

5.1 The first rainband

The first rainband occurs during the period from 2100-2300 HST on 7 August 1990. This is the first significant precipitation observed on the windward side of the island. To study the evolution of rainfall during this period, low beam elevation (0.5^o) surveillance scans (Fig. 5.2) from Hilo will be used to evaluate the rainshowers at far distances offshore. Chapter two describes some of the parameters of the radar used in HaRP. Because of the high pulse repetition frequency used to avoid velocity folding, the maximum unambiguous range is limited to 75 km. The results of range limitations can be seen in Figs. 5.2a and b. At 1800 HST (Fig. 5.2a) only a couple circular echoes exist far northeast of CP-4. By 1900 HST (Fig. 5.2b) more isolated echoes are indicated far northeast. The echoes at 1900 HST are probably not new, but have moved into the 75 km radar range. The echoes continue to move with the trade winds at 2000 HST (Fig. 5.2c) until they are located just offshore of the windward coast by 2100 HST (Fig 5.2d) The echoes circular appearance and their isolated coverage leave no doubt that these are trade-wind showers with no evidence of any bandlike structure before 2100 HST.

With the showers located just offshore, it is now necessary to use a higher radar beam elevation (4.5°) so the evolution of the echoes as they move over the island can be viewed without ground clutter. At 4.5°, the radar beam climbs over almost all of the island topography except for Mauna Kea. It is also useful at this time to see the echo evolution and surface wind field together to look for evidence of enhancement and focusing by the interaction between the downslope flow and trade winds. Such an analysis is at Fig. 5.3. At 2115 HST (Fig. 5.3a), the showers can be seen offshore. Some of the showers have already moved over the northern portions of the coast. Some of the stronger echoes (30 dBZ) are located offshore of Paradise Park (station 8), in addition to a cell very near the radar site at station 9. At this time, the wind data reveals that downslope flow has not yet reached the coast. 15 minutes later at 2130 HST (Fig. 5.3b), some of the echoes that were previously offshore are now moving over the coast. An area of 30-40 dBZ reflectivity is located directly over station 8. Recall that at this time, the PAM surface data indicated a gust front signal. The gust front, was likely produced by this echo area. 2145 HST (Fig. 5.3c) shoes the first evidence of significant enhancement of the showers. A solid line of 30 dBZ reflectivity is observed from northwest of station 13 extending southeast past station 8. That area matches well with the leading edge of the downslope flow at that time. It appears that as the showers encounter the downslope flow, they are enhanced and focused into a line. At 2200 HST (Fig. 5.3d), some weakening of the line is noticed as it continues to move inland. The solid 30 dBZ line has now broken up into 3-4 major segments.

The stronger radar echo (greater than 30 dBZ) seems to have an effect on the surface winds. In chapter 4, it was shown that, over the coast and lowlands, rainshowers tended to destroy the downslope flow and bring a return to easterly winds by vertical momentum transport. A relationship between reflectivity and surface winds can be seen in

40

Fig. 5.3c and d. At 2145 HST (Fig. 5.3c), just after the 30 dBZ line passes over station 13, the winds shift from downslope to an easterly direction. A similar situation occurs at 2200 HST (Fig. 5.3d) at stations 44 and 4. This apparent link between destruction of the downslope flow layer and stronger reflectivity is interesting. Since reflectivity is a proxy for rainfall rate, it can be speculated that vertical momentum transport is more effective in heavier rainshowers. Thus, with other factors being equal, stronger rainshowers may be more likely to cause a switch from downslope winds to easterly winds due to trade-wind momentum transport.

The continued inland march of the showers is shown in Fig. 5.4. The weakening of the line is evident at 2215 HST (Fig. 5.4a) and 2230 HST (Fig. 5.4b) as the 30 dBZ reflectivity areas continue to dissipate reflecting an overall weakening of the line. It appears that, although the intensity is decreasing, the size is still quite large indicating light precipitation over most of the windward side of the island. However, by 2245 HST (Fig. 5.4c) and 2300 HST (Fig. 4.4d) the entire echo system begins to dissipate leaving only one 30 dBZ reflectivity area north of station 15.

The enhancement of rainshowers was well defined as they moved over the coast and into lowland areas. This enhancement must be tied to the increased convergence as the showers in the trade-wind layer encounter the westerly winds along the drainage front. The rainfall produced by this band is reflected in Fig. 5.5. Although the showers underwent a significant enhancement after passing the coast, not a great deal of precipitation occurred during this period. In fact, the rainfall during 2100-2300 HST accounts for only about 10% of the total rainfall accumulation for 7-8 August 1990 (Fig. 5.1). The pattern in Fig. 5.5, however, is important. The narrow swath of over 1 mm of rainfall over the lowland

41

areas matches the orientation of the band as seen in Fig. 5.3c. This is strong evidence that enhancement and focusing of the showers has occurred in this area.

5.2 The second rainband

The second rainband occurs between 0300-0500 HST on 8 August 1990. Like the first rainband, inspection of radar echoes at far distance upstream will be conducted first. The radar scan at midnight (Fig. 5.6a) shows isolated showers located near the edge of the 75 km radar range far upstream. It is clear from the echo pattern at midnight and 0100 HST (Fig. 5.6b), that some rainshowers exist over the lowlands in addition to the showers upstream. At 0200 HST (Fig. 5.6c) a large echo area with 30 dBZ cores moves into radar range. This area then moves westward close to the coast by 0300 HST (Fig. 5.6d). The evolution of the echo pattern from 0200-0300 HST illustrates an important point. Like the first rainband, the echoes appear to be dissipating and regenerating as they track towards the island. No echoes have continuity from the edge of the radar range all the way to the coast. Instead, they experience discrete motion as new cells form and older cells dissipate. This makes tracking individual cells nearly impossible.

As the rainshowers near the coast at 0315 HST (Fig. 5.7a), they still have a scattered organization with several areas of 30 dBZ reflectivity. The showers cross the coast at 0330 HST (Fig. 5.7b) and begin to organize into a line at 0345 HST (Fig. 5.7c), and by 0400 a clear line develops extending in a north to south orientation from the northern coast to near station 4. The solid 30 dBZ line has isolated cores of near 40 dBZ.

Enhancement and focusing of the previously scattered rainshowers is again occurring over the lowlands.

Like the previous rainband, wind reversals from downslope flow to easterly flow begin to occur at coastal stations as the stronger echoes pass the station. This can best be seen at 0330 HST (Fig. 5.7b) at station 8. Here a windshift is indicated shortly after the band of nearly 40 dBZ echo reflectivity passes the station. This is remarkably similar to the apparent gust front at 2130 HST from the first rainband. Wind reversals also occur at 0400 HST (Fig. 5.7d) at stations 9, 44, and 4 as the line of showers passes over these stations. One key difference between this case and the previous rainband is the extent of the downslope flow. The first rainband encountered the drainage front over the lowlands, whereas the current case features downslope flow that extends offshore. It appears that in the 0300-0500 HST rainband, significant enhancement occurs only after the showers reach the lowlands (Fig. 5.7d). The downslope flow over the coast is destroyed by the showers through vertical mixing causing easterly winds over the coast which would tend to increase the convergence over the lowland areas (Figs. 5.7c and d). This leads to a large retreat in the drainage front, casing the most pronounced focusing and enhancement to occur there and not offshore when the showers initially encounter the drainage front.

The evolution of the rainband after 0400 HST shows that it remains largely intact but weakening starting at 0415 HST (Fig. 5.8a). The next couple of scans, at 0430 HST (Fig. 5.8b), 0445 HST (Fig. 5.8c), and 0500 HST (Fig. 5.8d) show the rainband progressing upslope with the line continuing to weaken and break up. At 0500 HST (Fig. 5.8d), another echo area offshore is poised to move over station 8 over the next hour. This echo appears to be the source of the rainfall near 0530 HST at station 8 that provides some

43

evaporative cooling along the coast and allows another resurgence of downslope flow to the coast.

The rainfall that accumulates from the second rainband (Fig. 5.9) is much greater than that observed in the first rainband (Fig. 5.5). This period represents about 40% of the total rainfall between 1900-0700 HST (Fig. 5.1). The rainfall pattern from 0300-0500 HST reflects a north-south orientation with a maximum accumulation of over 10 mm at station 23. The 4 mm contour has close agreement with the location of the rainband observed by CP-4 radar (Fig. 5.7d-5.8b). A relationship seems to exist between the swath of maximum rainfall accumulation and the enhancement of the scattered trade-wind showers into a line. It is significant to also note that the maximum rainfall occurs near the farthest westward retreat of the drainage front. This signifies the enhancement of the trade-wind showers by the interaction between the downslope flow and trade-winds along the drainage front.

CHAPTER SIX

SUMMARY

6.1 Conclusions and discussion

One of the goals of this study was to investigate the evolution of downslope flow on 7-8 August 1990 in the presence of strong trade winds and frequent trade-wind showers. From this investigation, it was learned that downslope flow evolved in a very untypical manner compared to normal HaRP conditions. With the afternoon hours relatively dry, downslope flow initiated on the upper slope by radiative cooling under an area frequently dominated by orographic cloud. Downslope flow then progressed down the slope to the windward lowlands also from radiative cooling. At this point, however, downslope flow was held up by the strong onshore trade-wind flow at the coast similar to the 10 August 1990 case (Feng and Chen 1996).

Downslope flow arrival at the coast occurred much later than HaRP mean conditions. Unlike the 10 August 1990 case, downslope flow at the coast was not initiated by the gradient caused by cold pool over the lowlands and the warm trade-wind environment at the coast. Instead, downslope flow was observed only after a band of precipitation moved over the coast producing evaporatively cooled air in the lowest levels and allowing downslope flow to extend offshore.

In addition to the evaporative cooling along the coast, the band of showers had interesting effects on lowland stations. As precipitation fell on stations that were under downslope flow, the showers seemed to bring back easterly trade-winds. The destruction of downslope winds was caused by vertical momentum transport of strong easterly winds

45

in the trade-wind layer overcoming the weak westerly downslope flow layer by mixing from rainshowers. This usually produced an increase in temperature and moist static energy at the surface as the potentially warmer air was brought down to the surface. This was also observed during the second rainband over both coastal and lowland areas. Over two rain periods, a repeatable signal was becoming evident. Rainfall occurring when the coast was experiencing trade winds produced evaporative cooling below cloud base. This evaporation at the surface and aloft was responsible for allowing downslope flow to extend offshore on two occasions. Rainfall over stations that are under downslope flow, however, tended to produce warming at the surface in the presence of vigorous vertical mixing.

The destruction of downslope flow and reestablishment of the drainage front inland is inextricable linked to the observed rainbands. It is interesting to note that even through isolated showers occur over stations experiencing downslope flow between the periods of rainbands, no significant return of easterly winds was noticed. In fact, the heaviest showers fell over station 8 between the two rainbands, but did not result in a windshift to easterly flow. As revealed in the radar data, wind shifts from downslope flow to easterly winds seemed to occur only when the well organized heavier showers within the band moved over stations under downslope flow. There seems to be some additional forcing from the organized band, perhaps through the generation of a propagating gust front. Isolated showers, regardless of the vigor of their vertical mixing, do not produce a windshift.

Another goal of this study was to determine the source of the observed rainfall. Through radar, it appears that most of the rainfall on 7-8 August 1990 comes from trade-wind showers from the ocean. The timing of the heaviest rainshowers matches the location of the disturbed area of trade-wind cumuli first discussed in chapter 3. This agrees

46

well with a study of summer trade-wind rainfall by Larson (1978) who suggested that most rainfall is from sub-synoptic scale disturbances moving over the island in the trade-wind flow.

The interaction between trade-wind showers and downslope flow is truly binary. The effects of the showers on downslope flow is well defined. The downslope flow, however, also has an effect of the trade-wind showers. Radar scans showed the trade-wind showers organizing into lines as they pass over the coast and lowland areas. It appears that there is some focusing and enhancement brought about by the increased convergence as the showers meet the drainage front. This interaction, however, is complicated since at the same time the showers are enhanced by the downslope flow, the mixing associated with the showers destroys the downslope flow and reestablishes a drainage front further inland.

6.2 Future work

This study revealed that the precipitation observed on 7-8 August 1990 was largely due to a disturbed area of trade-wind showers drifting over the island. Since it was shown in this case that the rainshowers were preexisting, one has to wonder if this process occurs frequently and is the true genesis of the morning rainbands. It is clear from this study that rainshowers exist well upstream of the convergence zone between downslope flow and trade winds. Thus, the explanation of rainbands having their genesis in this convergence zone is unacceptable. A better understanding of rainbands and their contribution to windward rainfall is necessary. It seems that radar is the best platform in monitoring the evolution of precipitation there. A complete radar climatology during HaRP needs to be accomplished to gain more insight into the genesis of rainbands.

MARWINSONDES   RADIOSONDES

VIDEO CAMERAS

NASA DC-8

Rainband(s)

Lee Vortex

2 TETHERSONDES

Trade Inversion

NCAR ELECTRA

50 PAMS

DUAL-DOPPLER (CP3 & CP4)

Convergence Zone

4 BUOYS

MOANA WAVE

915 MHz PROFILER
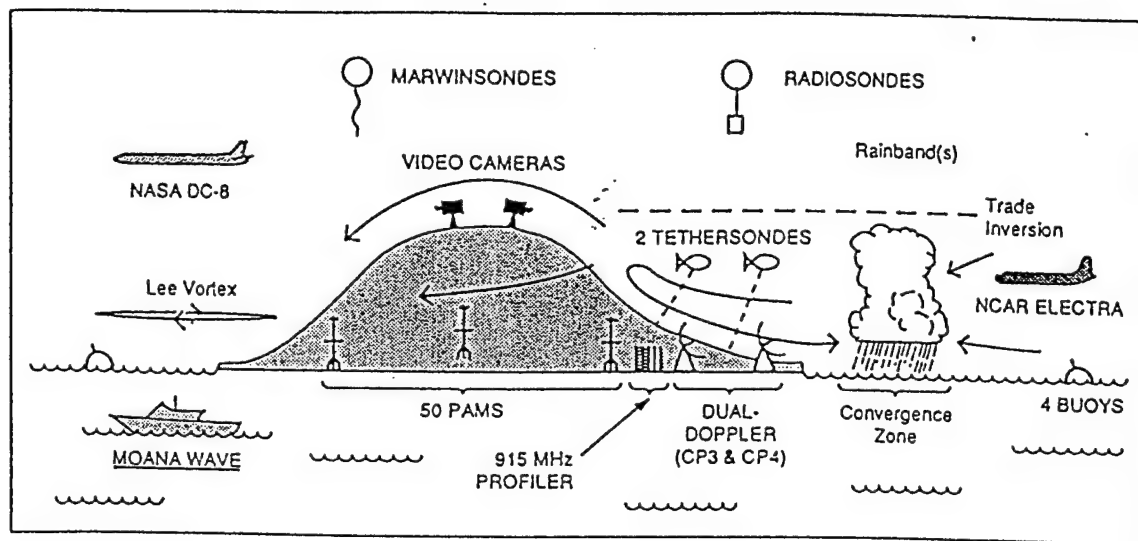
Fig. 1.1   Schematic representation of observing systems used in HaRP (illustration by Lee Fortier, NCAR).

48
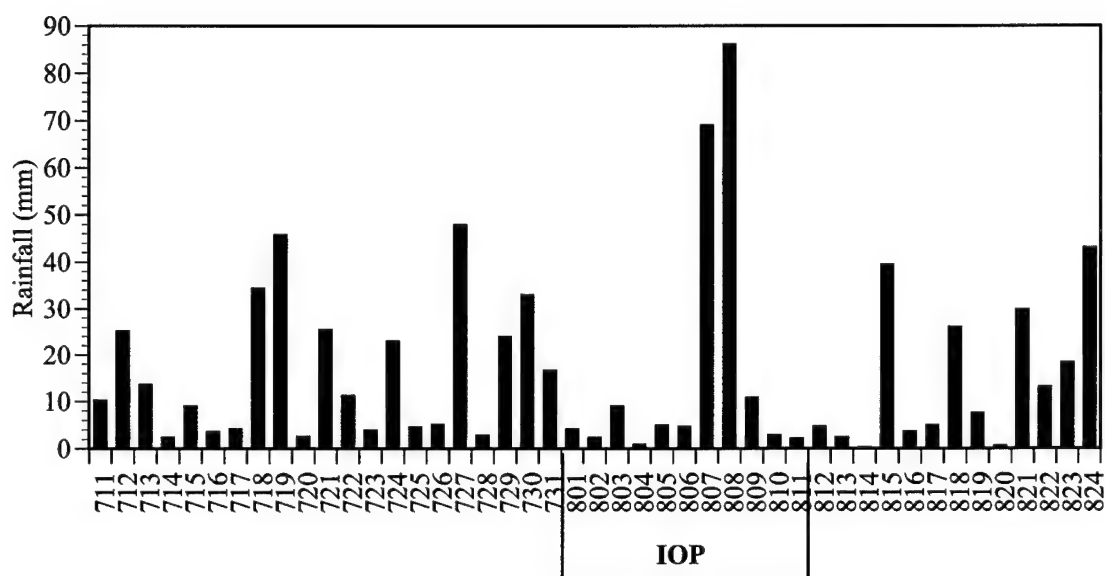
Fig. 1.2   Total rainfall (mm) from 03-07 HST for windward PAM stations (4, 5, 6, 7, 8, 9, 10, 11, 12, 13, 16, 22, 23, and 44) during HaRP.
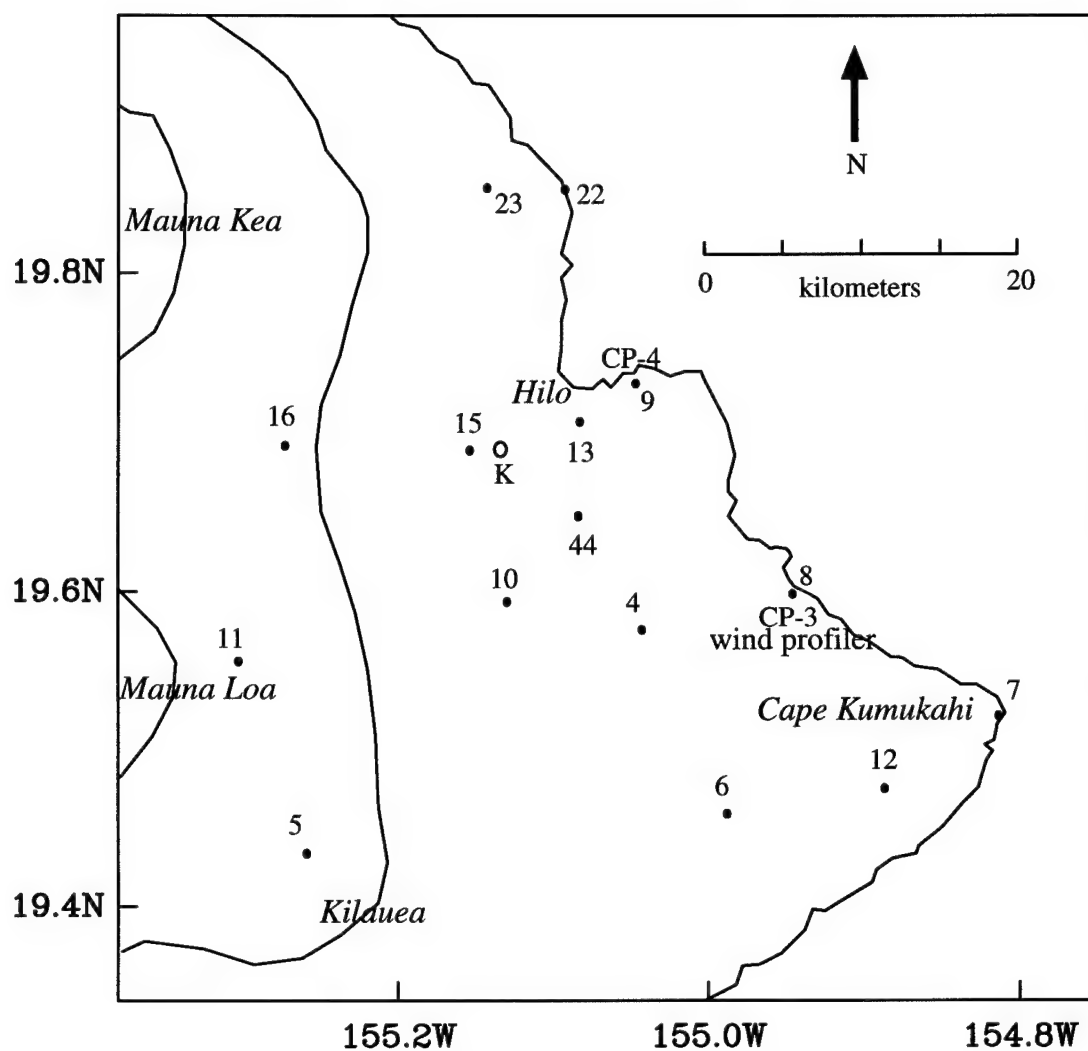
Fig. 2.1   Windward Hawaii with PAM sites (solid circles with station number), the
tethersonde site at Kaumana Elementary School (open circle), Doppler
radar locations, and profiler location. Contour interval for elevation is 1000
meters.
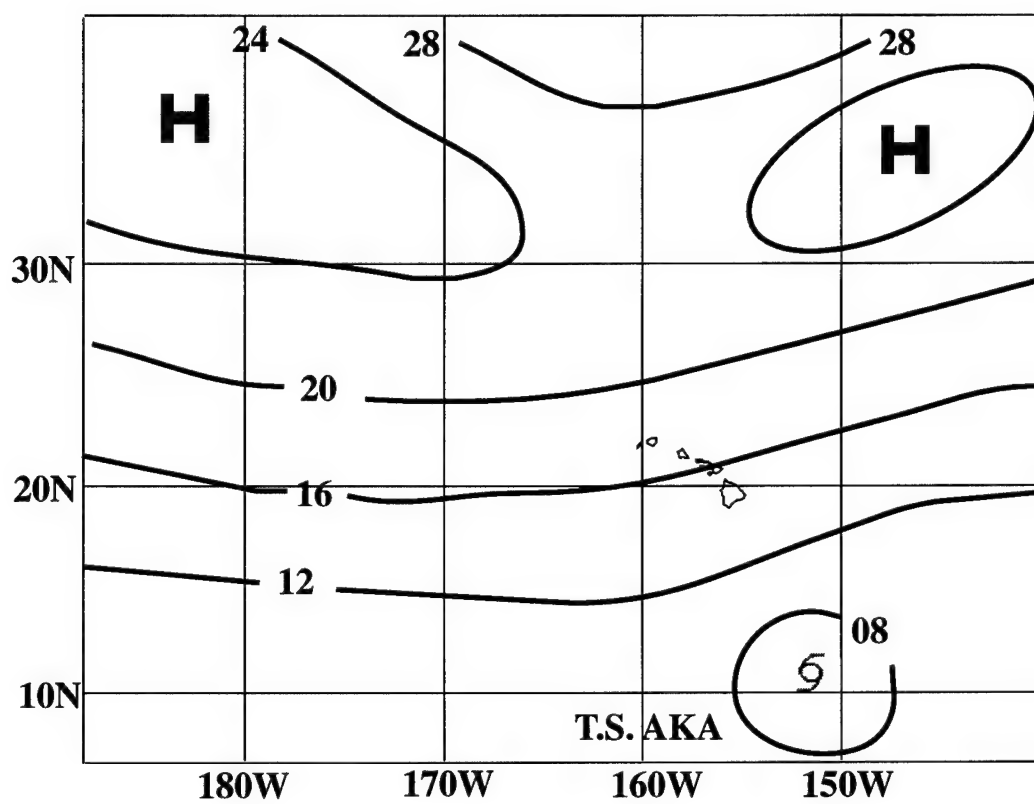
Fig. 3.1   Surface pressure analysis (P-1000 hPa) at 1400 HST on 7 August 1990.
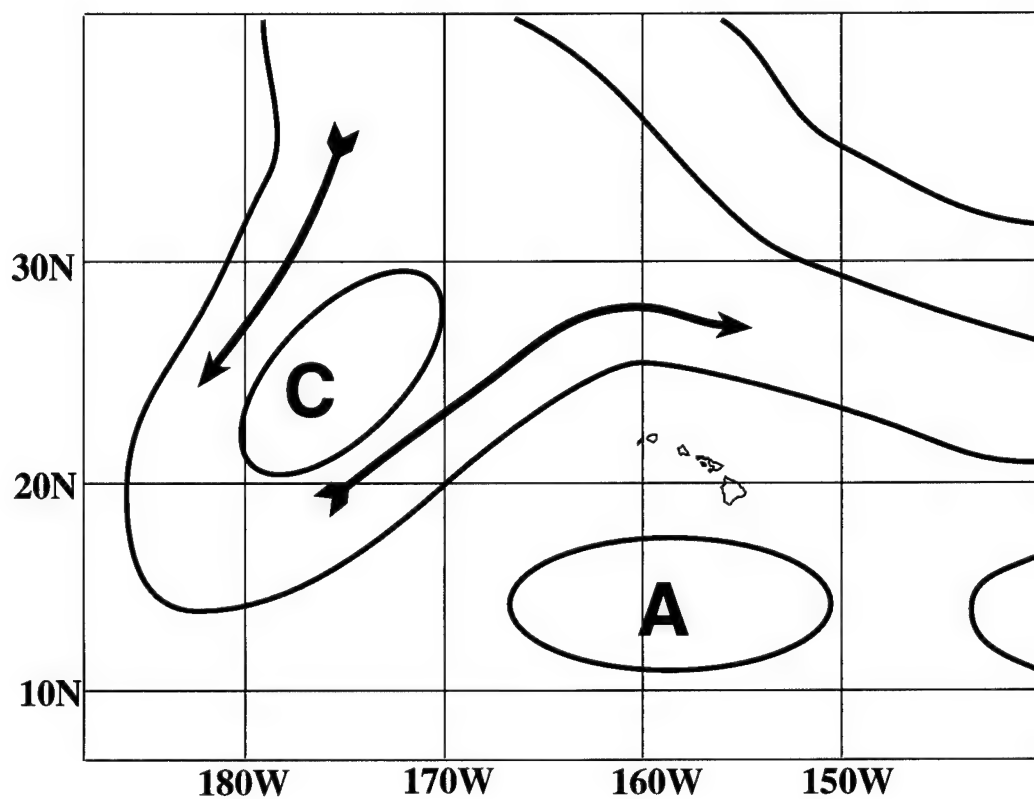
Fig. 3.2   250 hPa analysis at 1400 HST on 7 August 1990. Arrow represents 25 m s^{-1}
            winds.
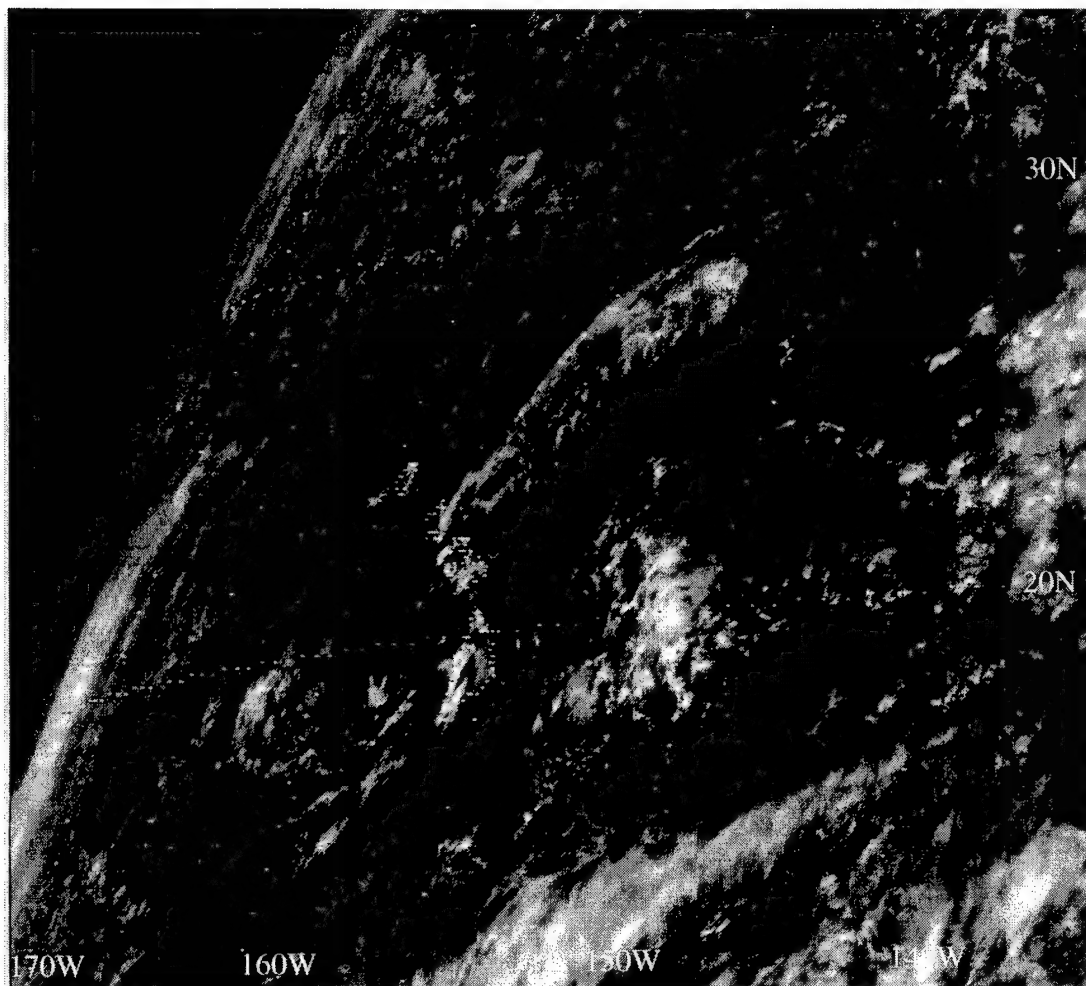
Fig. 3.3   GOES West visible satellite image at 1331 HST on 7 August 1990.
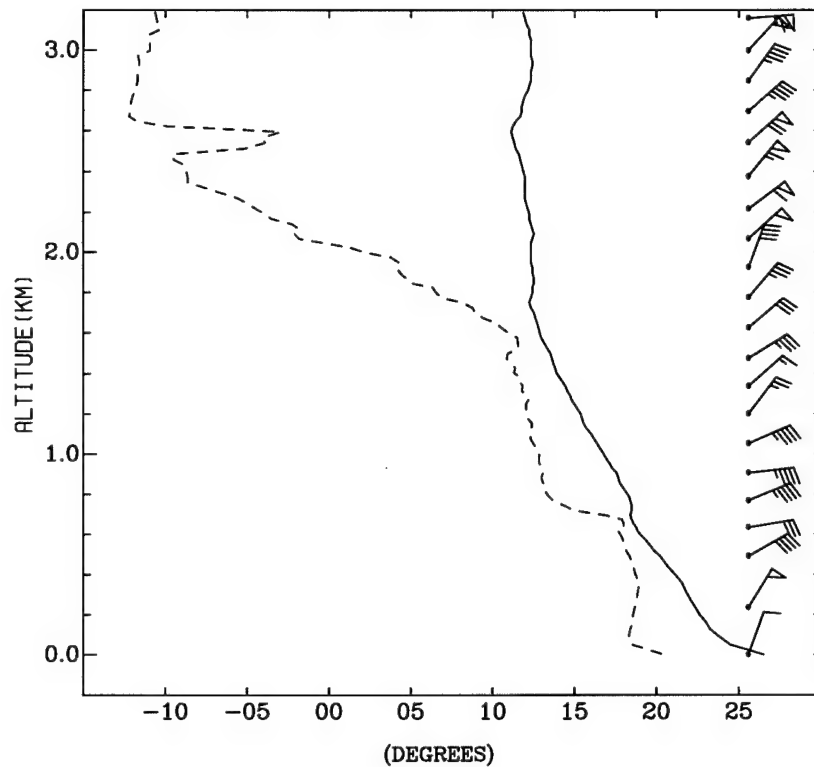
Fig. 3.4   Hilo sounding taken at 1400 HST on 7 August 1990. Solid line is temperature
(°C) and the dashed line is dewpoint (°C). Winds (m s⁻¹) with one pennant,
full barb, and half barb represent 5, 1, 0.5 m s⁻¹, respectively. The same con-
vention will be used for all wind profiles hereafter.

54
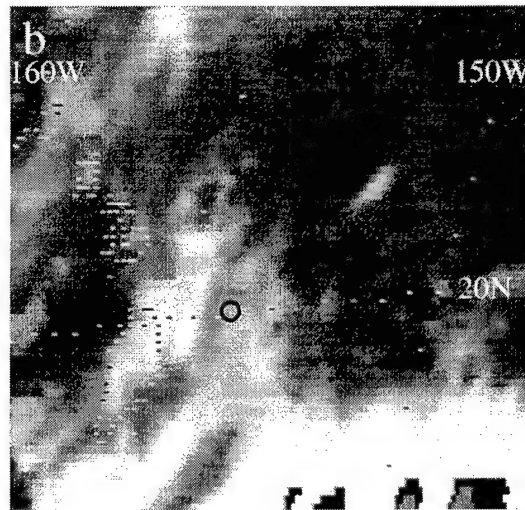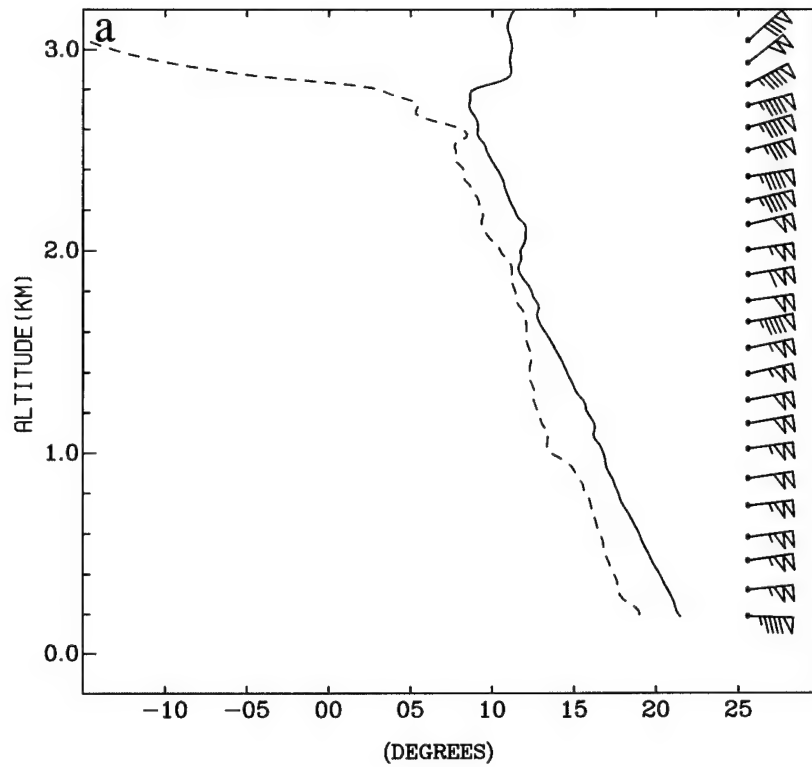
Fig. 3.5 (a) Same as Fig. 3.3 but for aircraft sounding taken approximately 140 km upstream starting at 2100 HST on 7 August 1990; and (b) GOES West IR satellite image at 2130 HST, open dot represents approximate location of aircraft sounding.
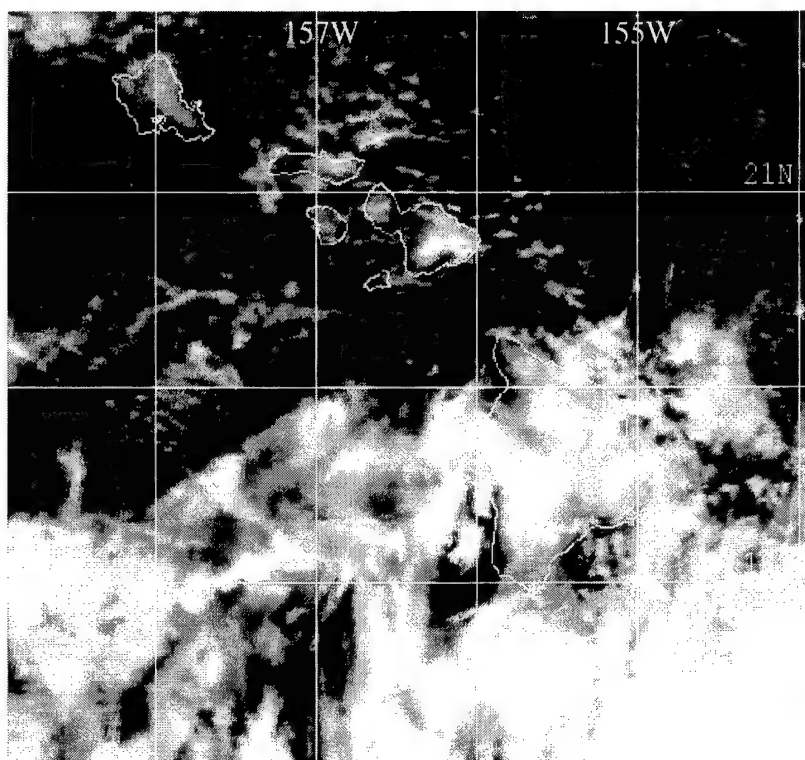
Fig. 3.6   NOAA-11 IR satellite image at 0208 HST on 8 August 1990.
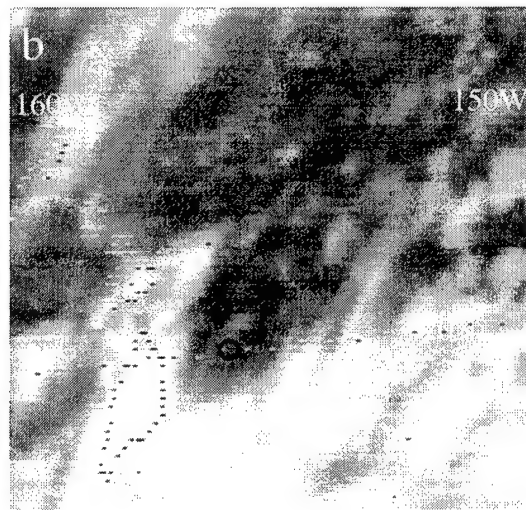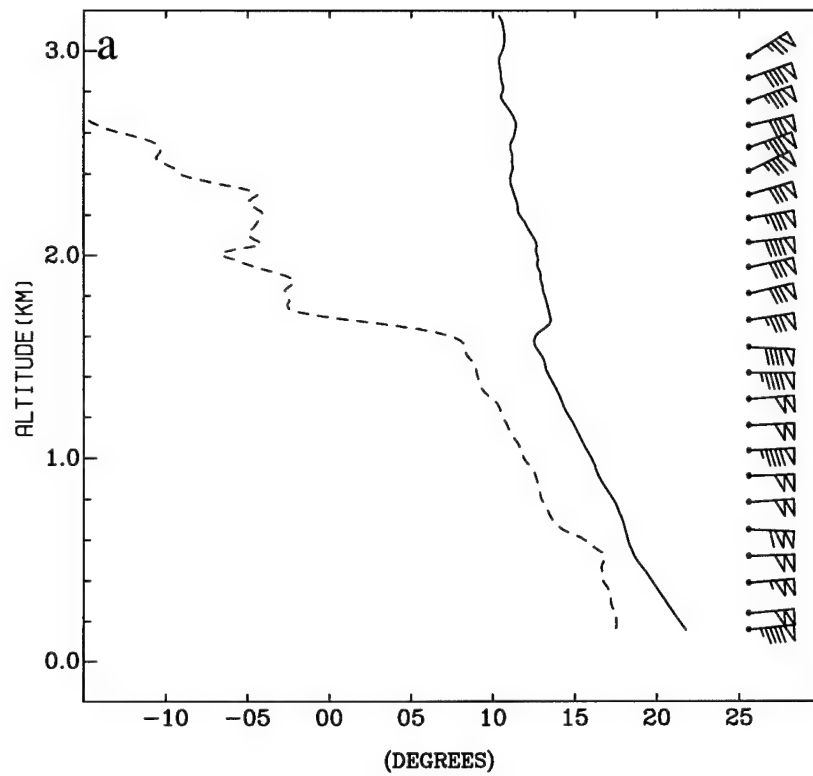
Fig. 3.7 Same as Fig. 3.5 but (a) aircraft sounding at 0400 HST on 8 August 1990; and (b) satellite image at 0430 HST.
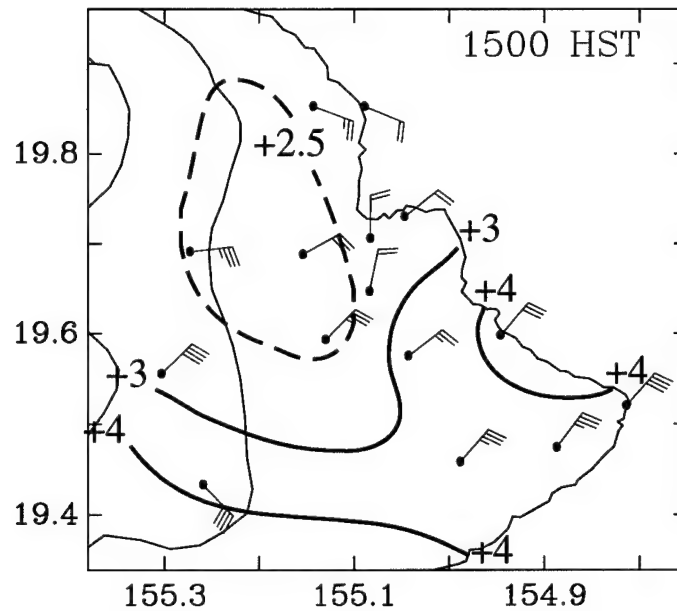
Fig. 4.1   Averaged surface winds at 1500 HST and PAM surface virtual temperature
(K) at 1500 HST minus the virtual temperature (K) of the aircraft sounding at
the same altitude approximately 150 km upstream. Wind (m s^{-1}) with one
pennant, full barb, and half barb representing 5, 1, and 0.5 m s^{-1}, respectively.
Hereafter, the same convention will be used for all figures.
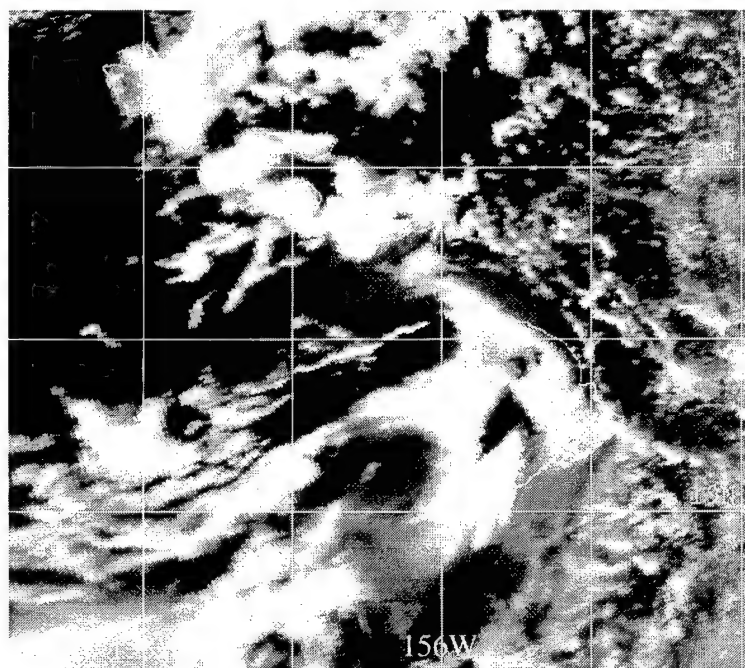
Fig. 4.2 NOAA-11 visible satellite image at 1335 HST on 7 August 1990.
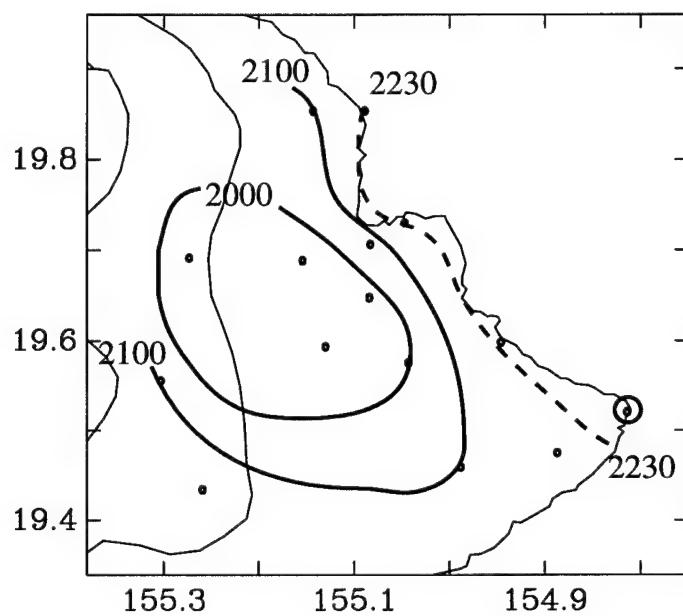
Fig. 4.3   Isochrone analysis of onset of downslope flow on 7 August. Time is HST.
Circle indicates station with no windshift.
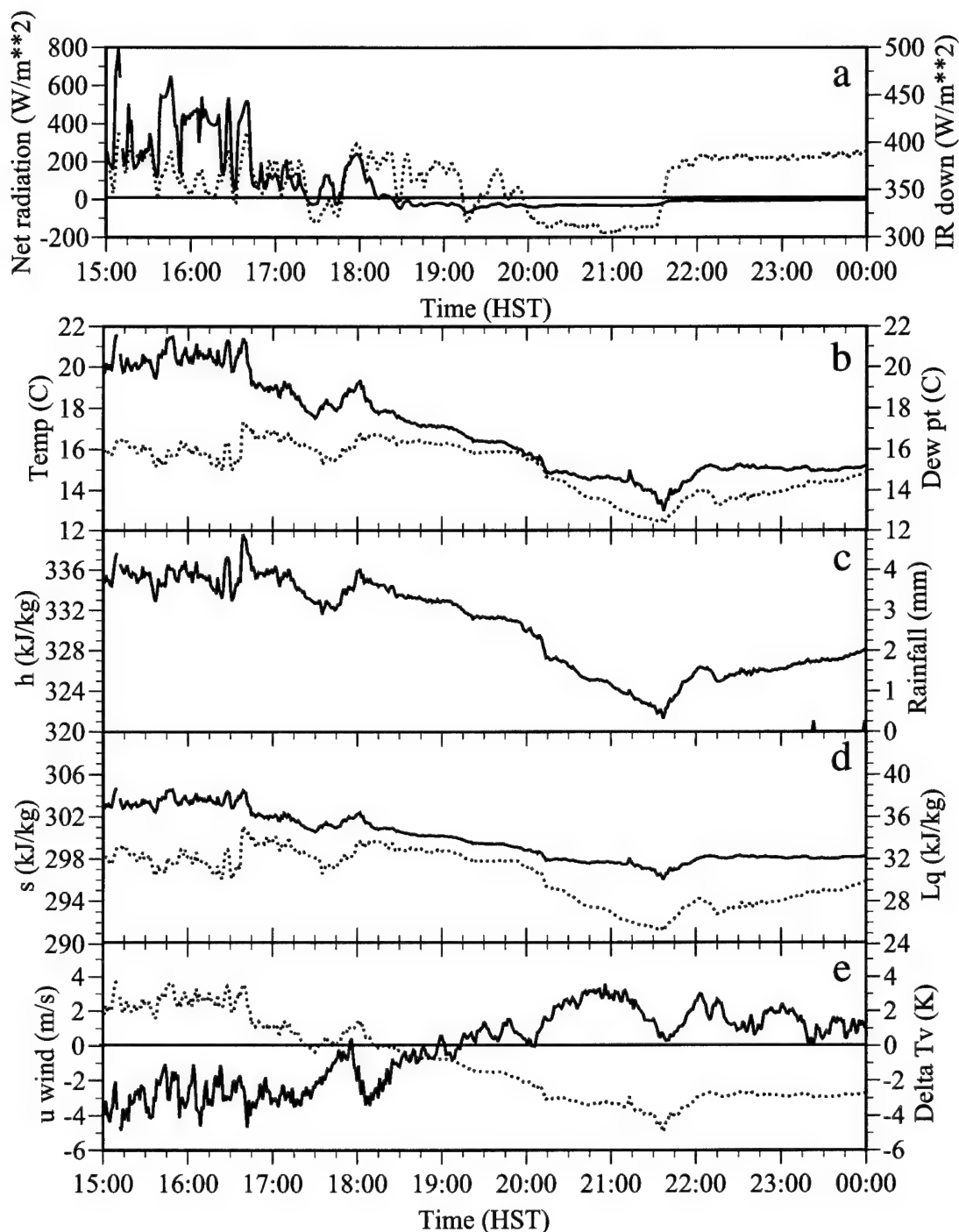
Fig. 4.4   Time series (1 min interval) of PAM data at station 16 on 7 Aug from 1500
to 0000 HST. (a) net radiation (W m^{-2}) (solid line) and downward infrared radia-
tion (W m^{-2}) (dotted line); (b) temperature (°C) (solid line), dew point (°C) (dot-
ted line); (c) moist static energy (kJ kg^{-1}) and rainfall (mm); (d) dry static energy
(kJ kg^{-1}) (solid line) and Lq (kJ kg^{-1}) (dotted line); (e) zonal component of sur-
face wind (m s^{-1}) (solid line) and difference in virtual temperature (K) (dotted
line) between PAM station and upstream aircraft sounding at the same elevation.

61
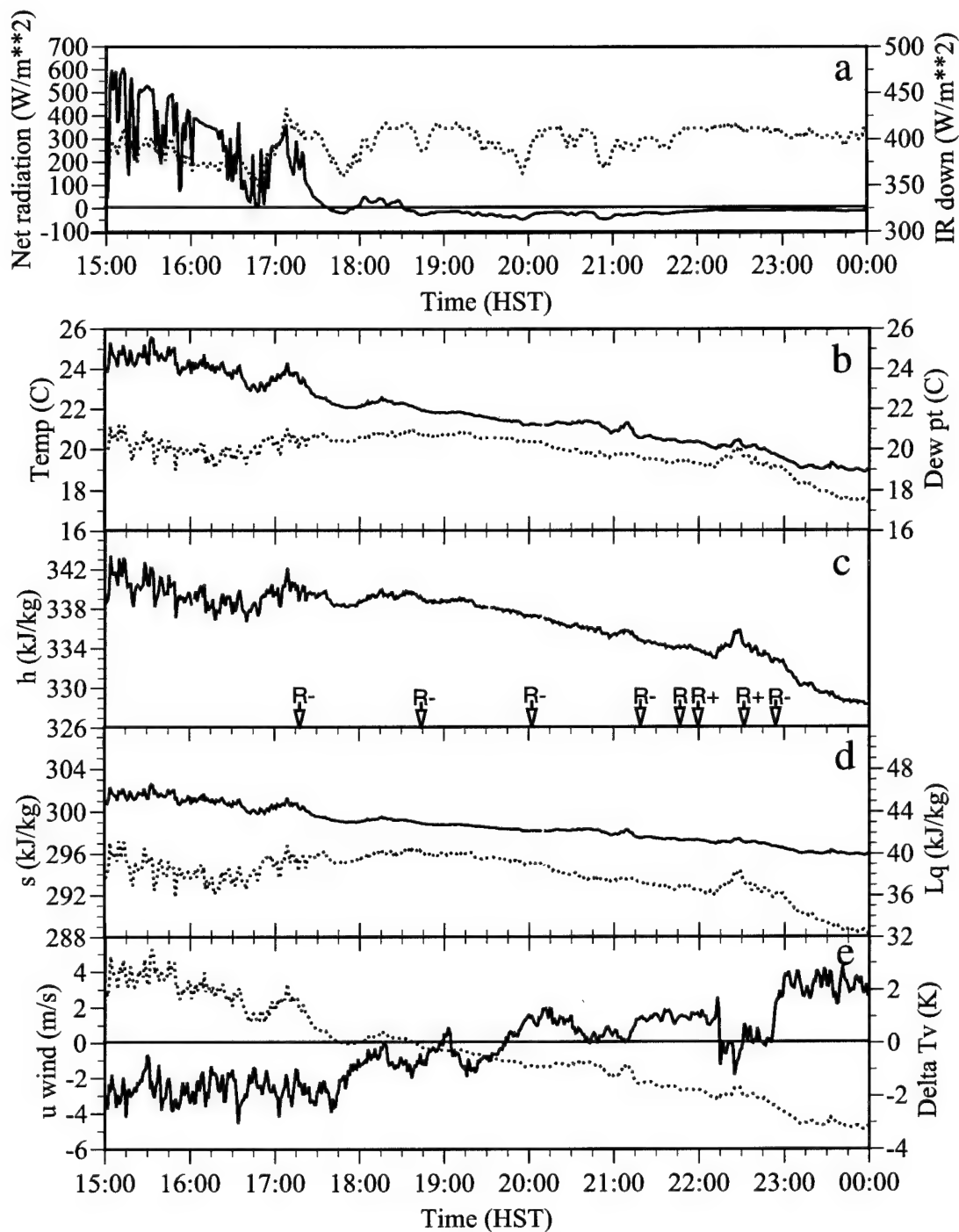
Fig. 4.5   Same as Fig. 4.4 but at station 15 (rainfall data from tethersonde log at Kaumana Elementary School).

62
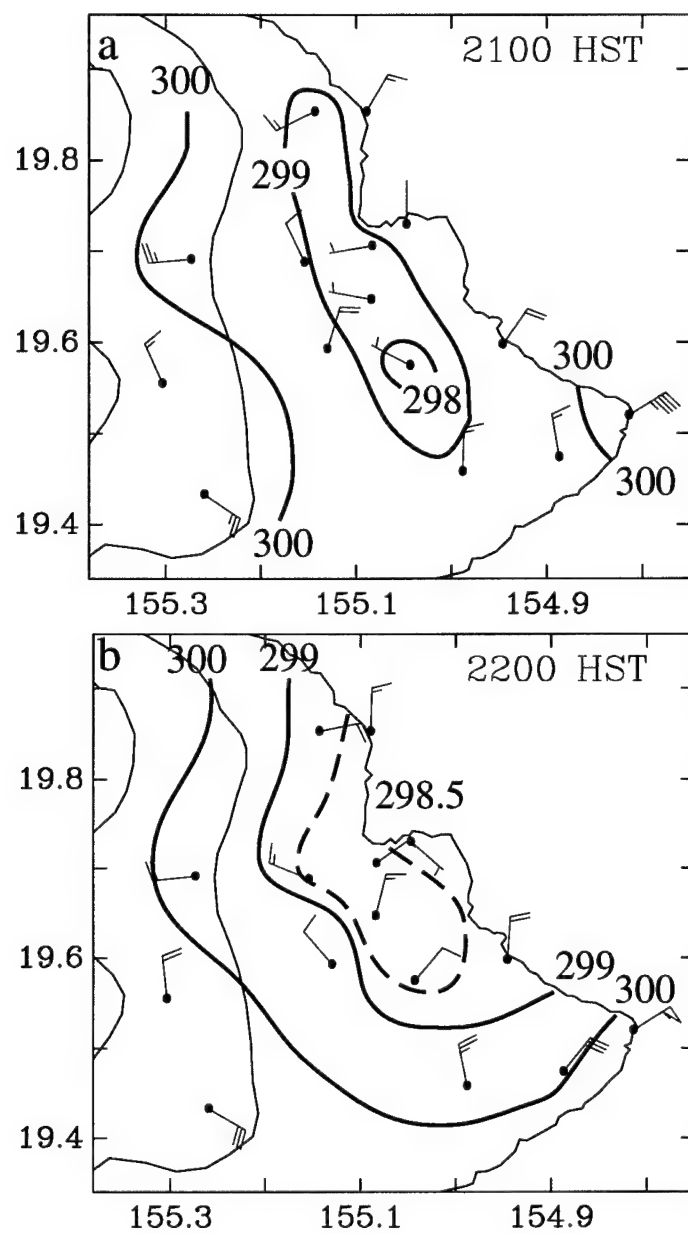
Fig. 4.6   Averaged surface winds (m s^{-1}) and surface virtual potential temperature (K) at (a) 2100 HST; and (b) 2200 HST.

63
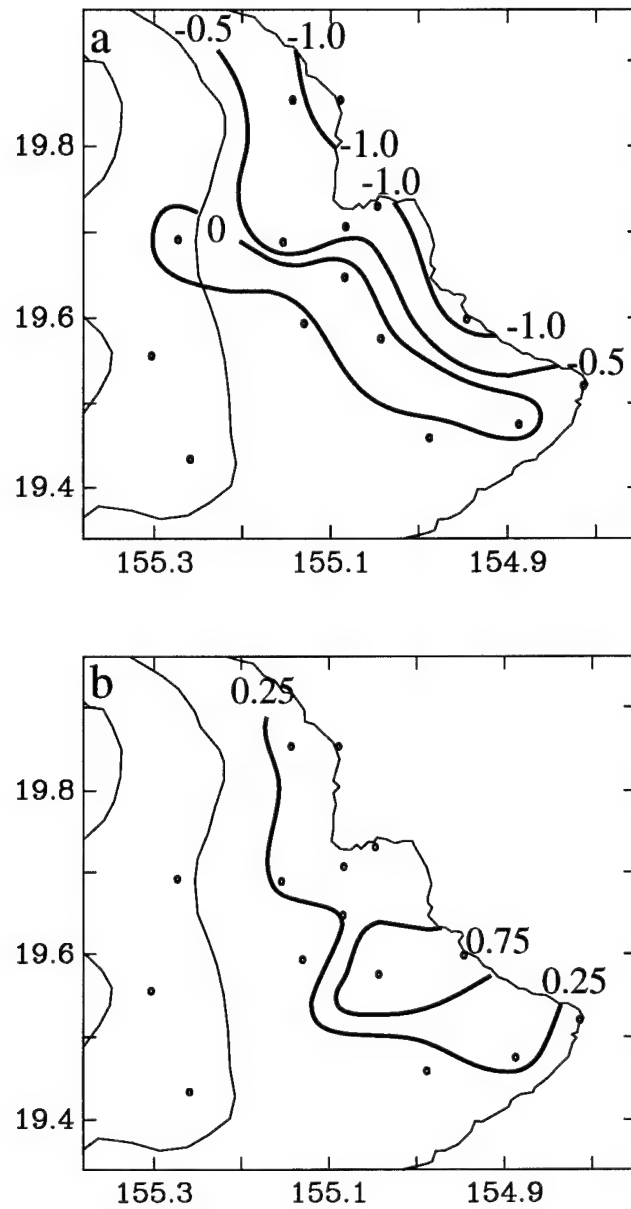
Fig. 4.7   For 7 August 1990, (a) the change in PAM virtual potential temperature
(K) from 2100-2200 HST and; (b) accumulated rainfall (mm)
between 2100-2200 HST.
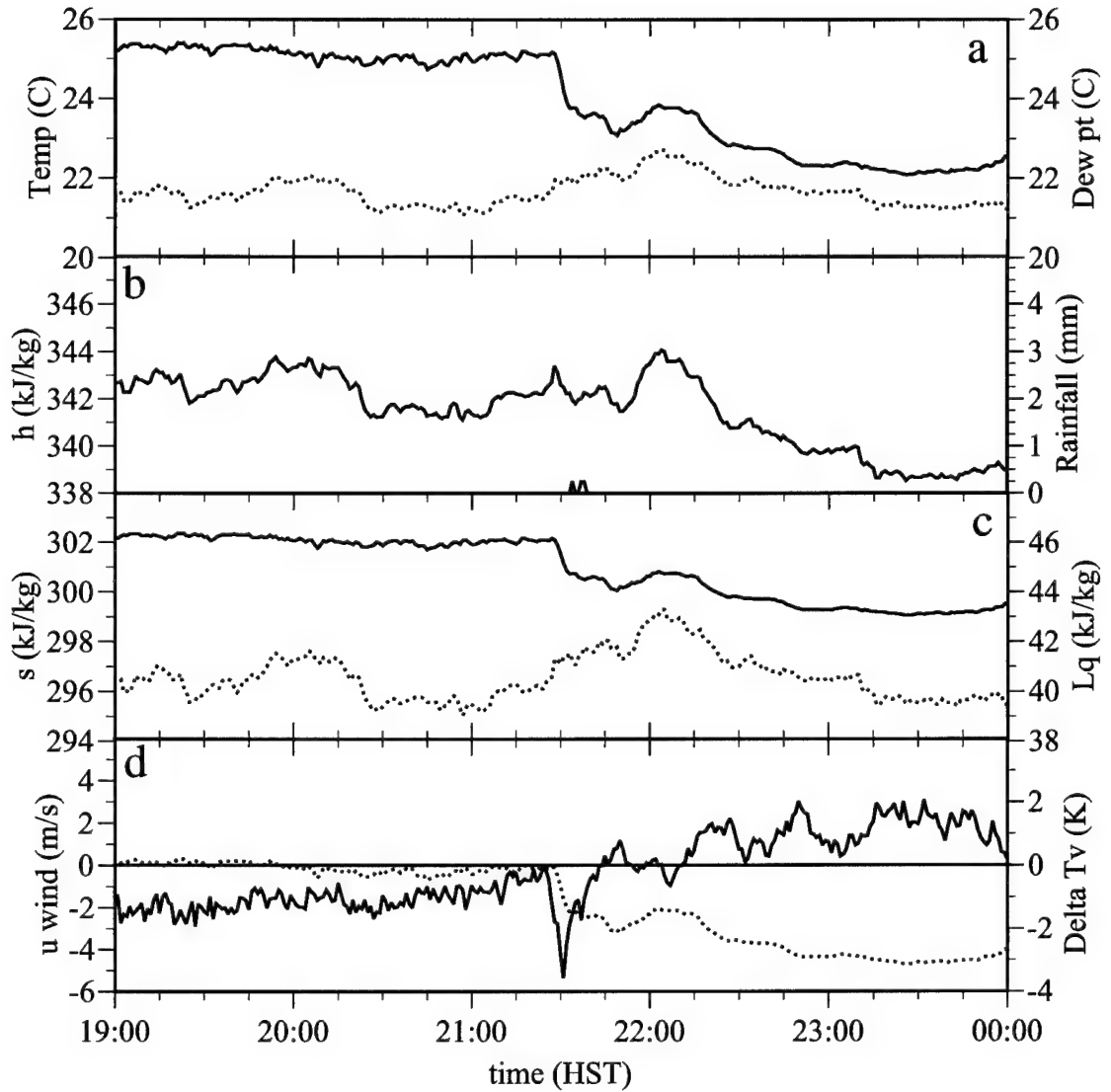
Fig. 4.8   Time series (1 min interval) of PAM data at station 8 on 7 Aug from 1900 to 0000 HST. (a) temperature (°C) (solid line), dew point (°C) (dotted line); (b) moist static energy (kJ kg^{-1}) and rainfall (mm); (c) dry static energy (kJ kg^{-1}) (solid line) and Lq (kJ kg^{-1}) (dotted line); (d) zonal component of surface wind (m s^{-1}) (solid line) and difference in virtual temperature (K) (dotted line) between PAM station and upstream aircraft sounding at the same elevation.
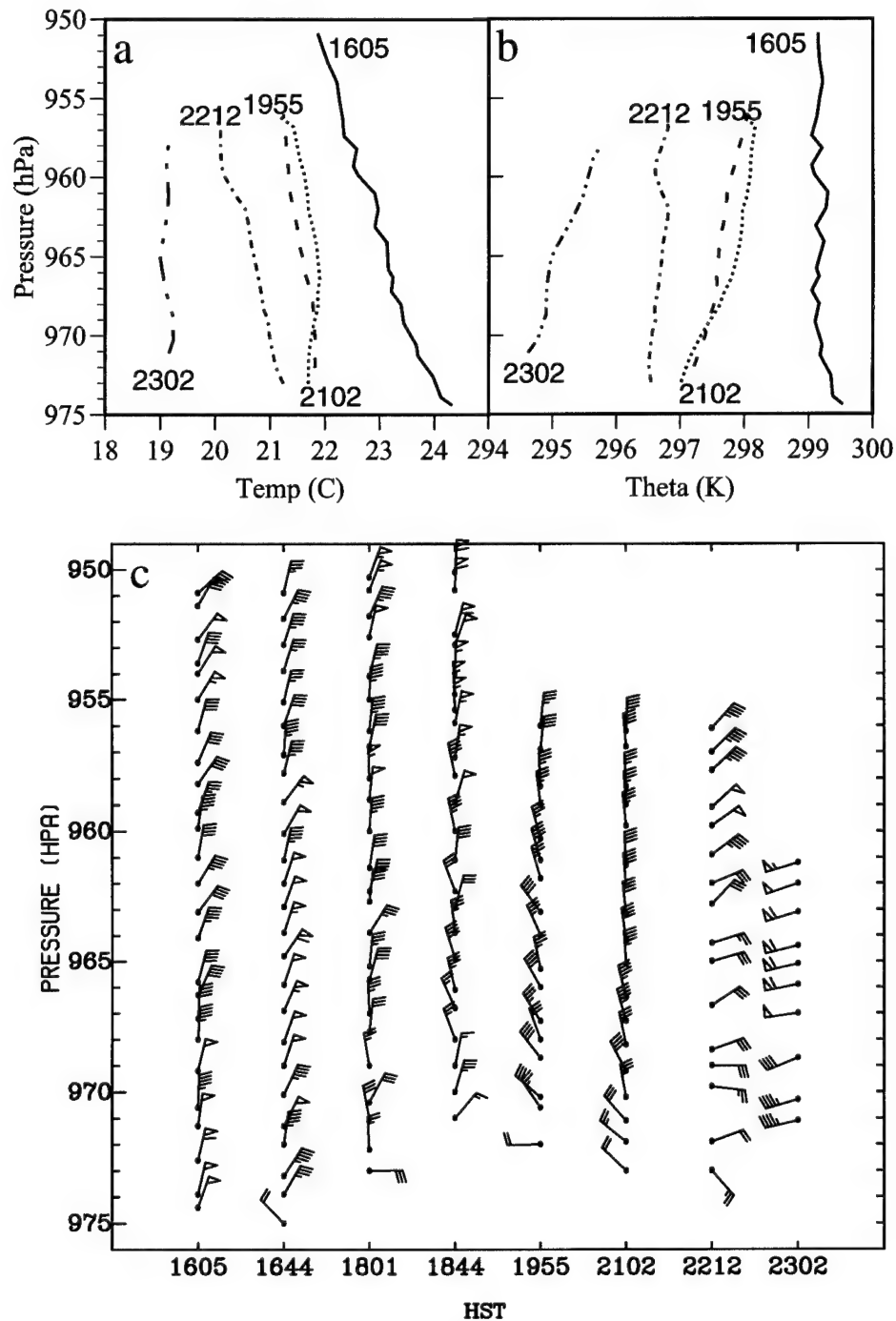
Fig. 4.9 Tethersonde soundings taken at Kaumana Elementary School on 7 August 1990, (a) temperature (°C) and (b) potential temperature (K) at 1605 HST (solid line), 1955 HST (dahed line), 2102 HST (dotted line), 2212 HST (dash-dotted line), 2302 HST (dash-double dotted line); (c) wind profiles (m s⁻¹).
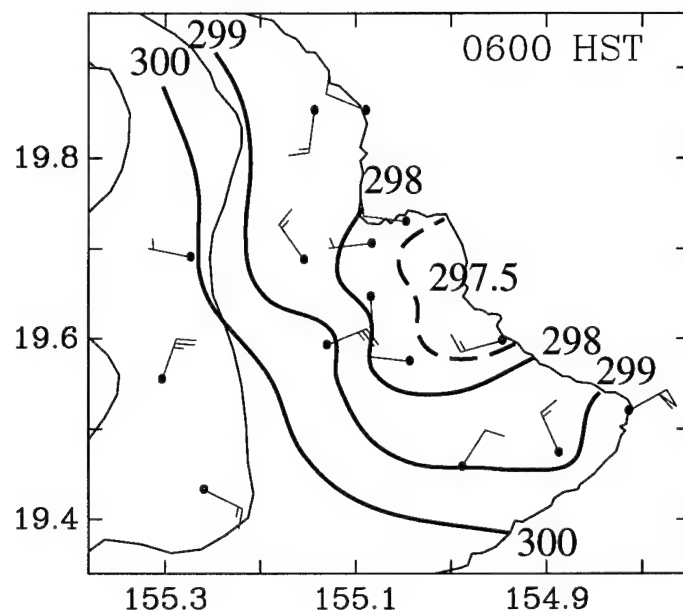
66
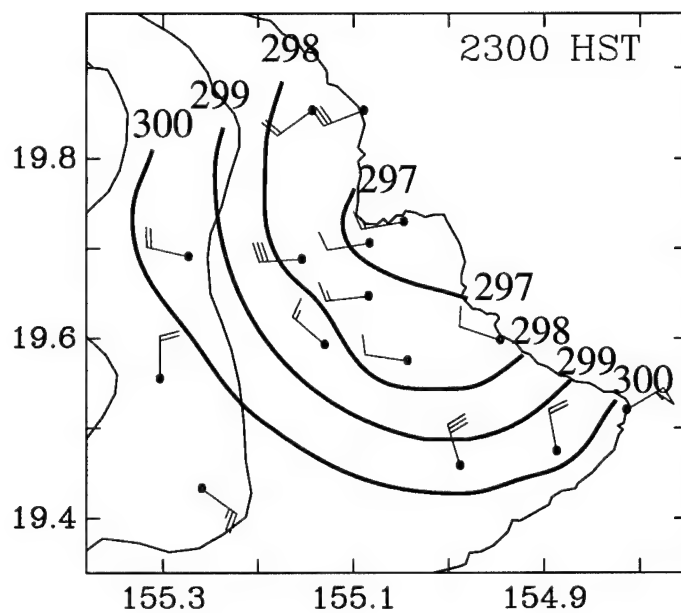
Fig. 4.10 Same as Fig. 4.6 but at 2300 HST.

67
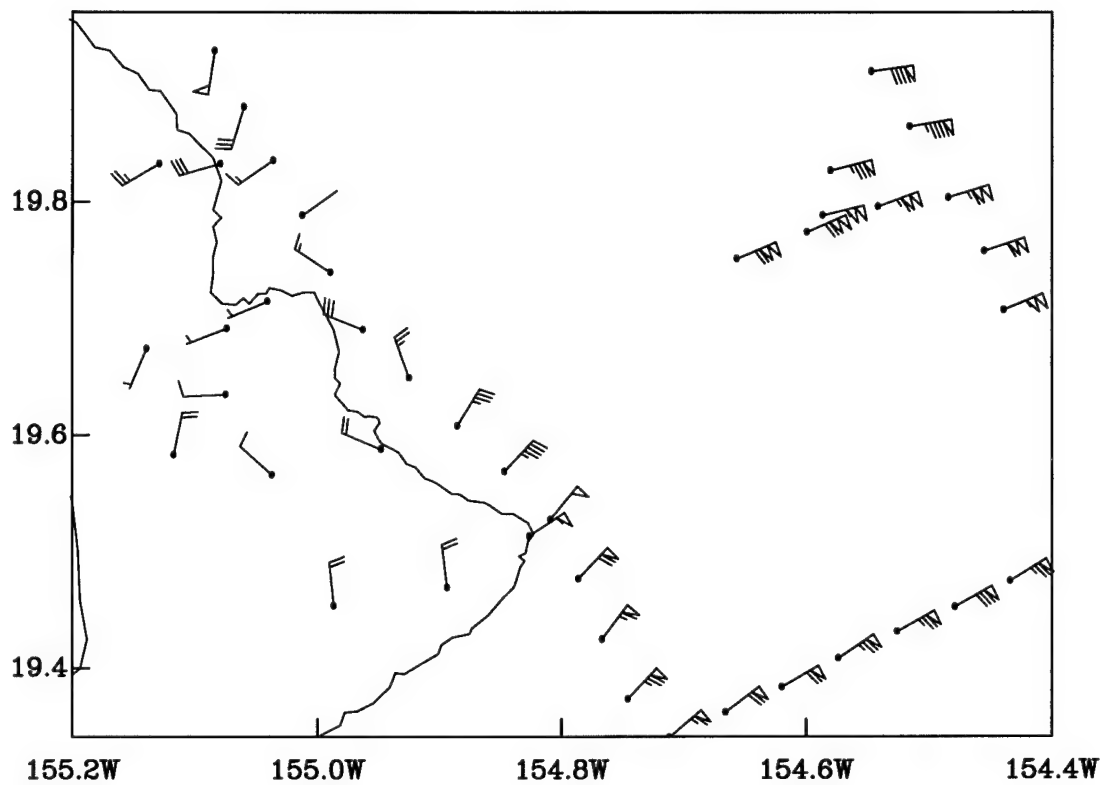
Fig. 4.11 Aircraft measured winds between 150-200 m between 2228-2300 HST. PAM data same as Fig. 4.1 but at 2245 HST.
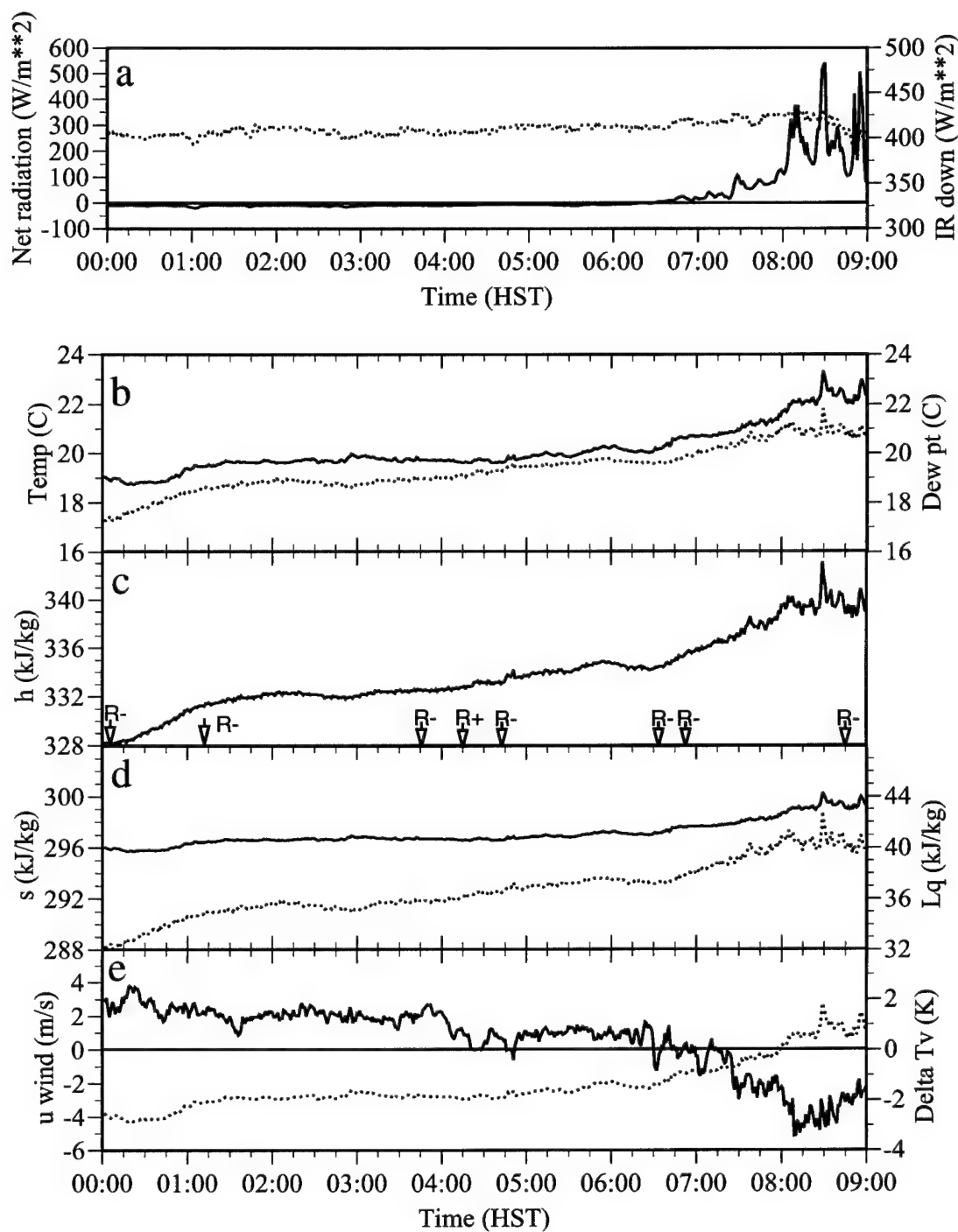
Fig. 4.12 Same as Fig. 4.5 at station 15 but from 0000-0900 HST on 8 August 1990.

69
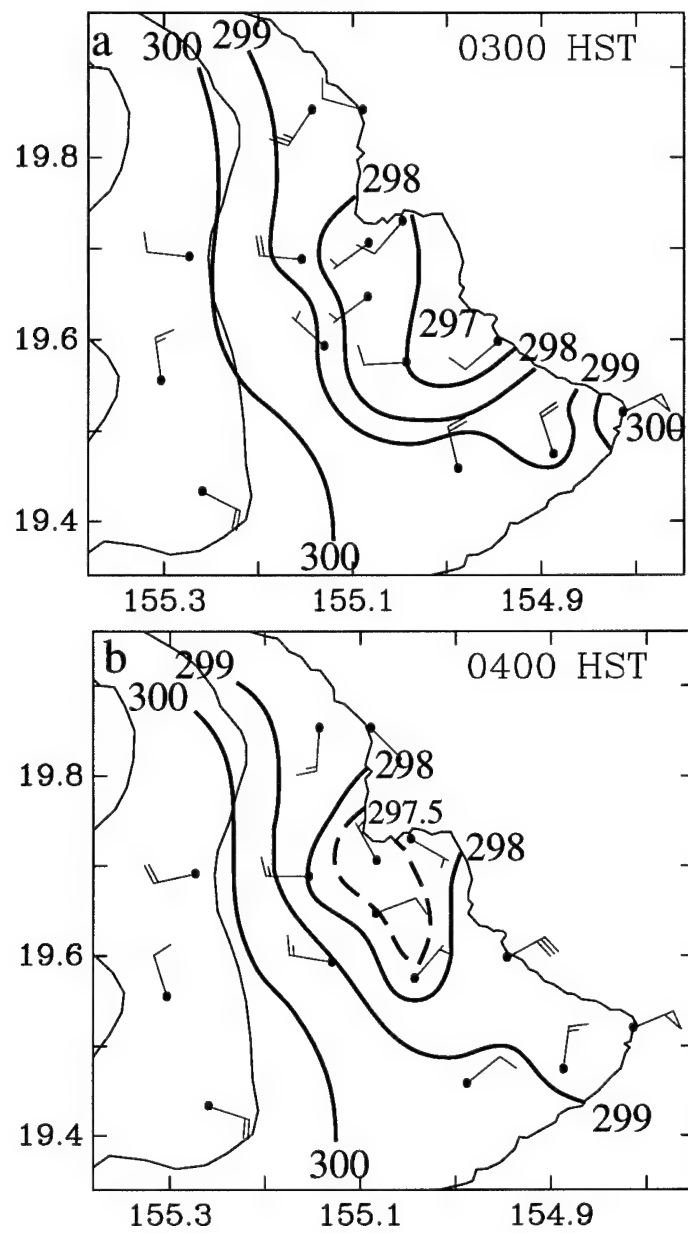
Fig. 4.13 Same as Fig. 4.6 but at (a) 0300 HST and (b) 0400 HST.
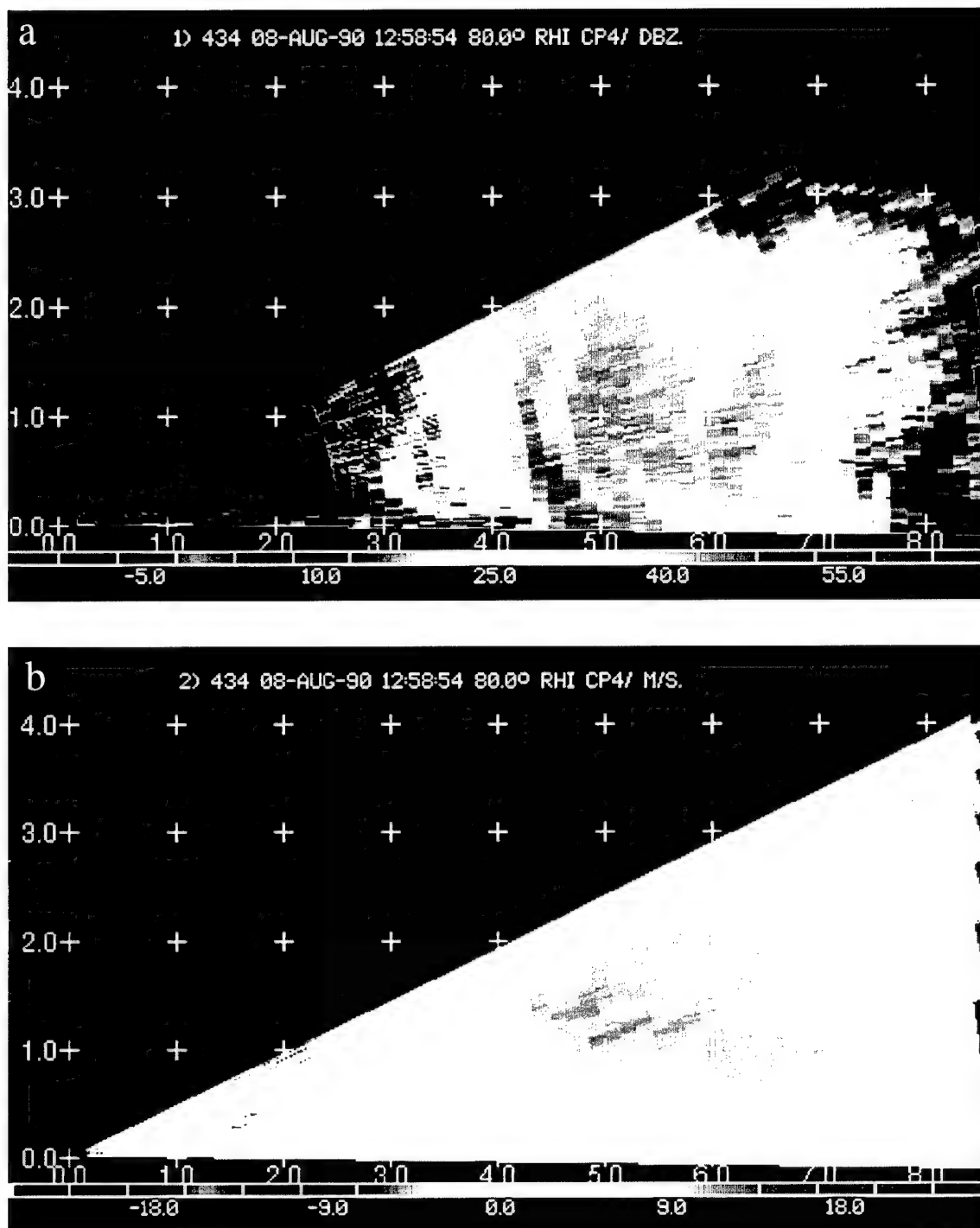
Fig. 4.14 Vertical cross section from RHI scan along 80° azimuth from CP-4 at 0258 HST on 8 August (a) reflectivity (dBZ), and (b) radial velocity (m s⁻¹)
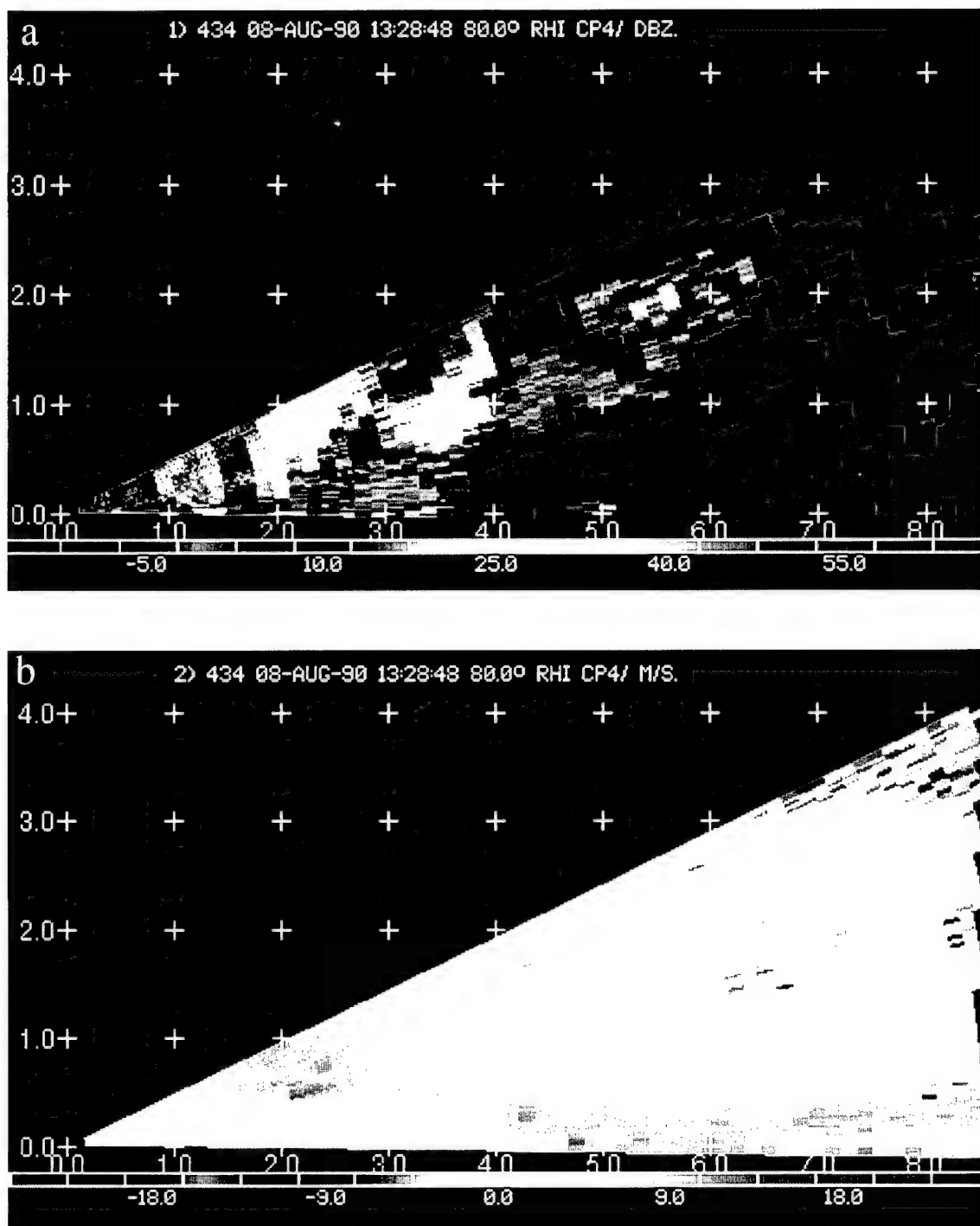
Fig. 4.15   Same as Fig. 4.14 but at 0328 HST on 8 August 1990 (a) reflectivity (dBZ),
and (b) radial velocity (m s^{-1})

72
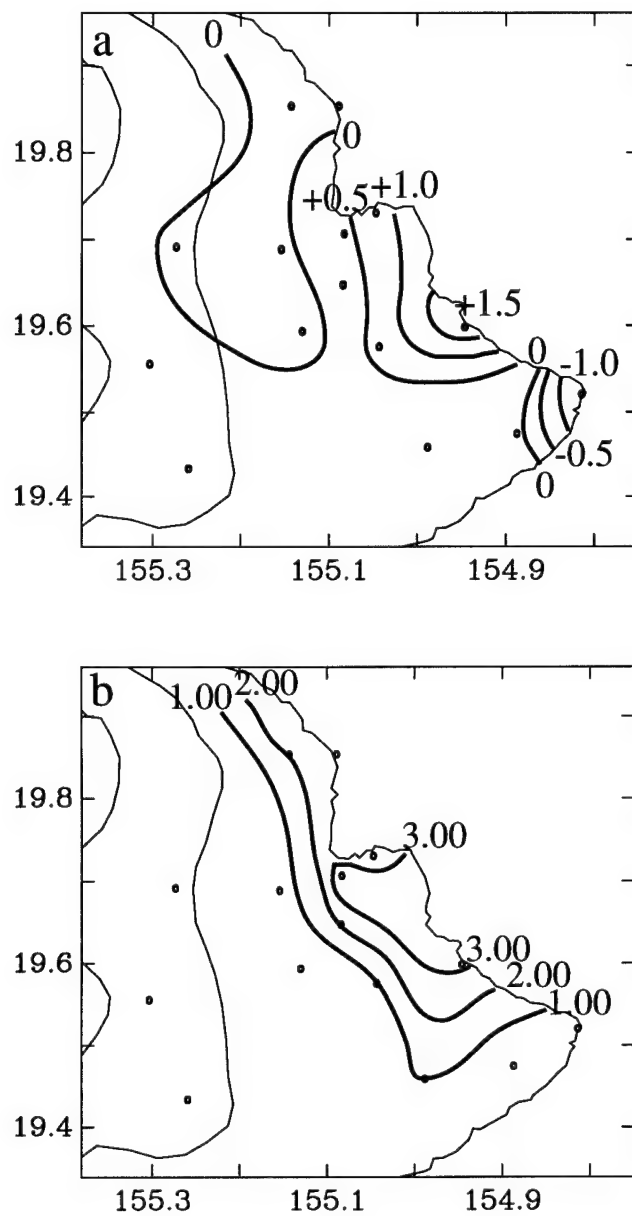
Fig. 4.16 Same as Fig. 4.7 but from 0300-0400 HST.
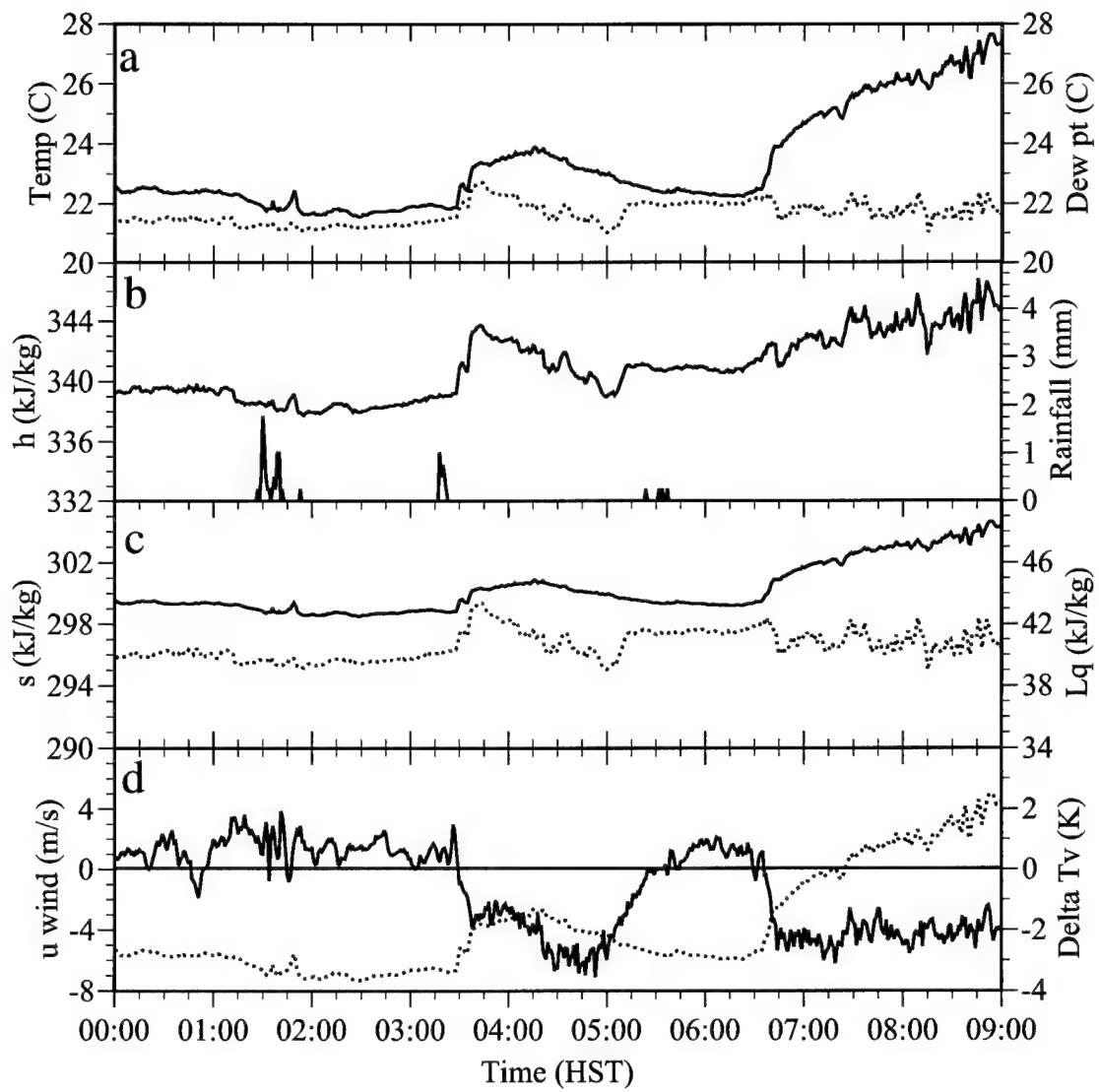
Fig. 4.17 Same as Fig. 4.8 but for station 8 on August 8 from 0000 HST to 0900 HST.
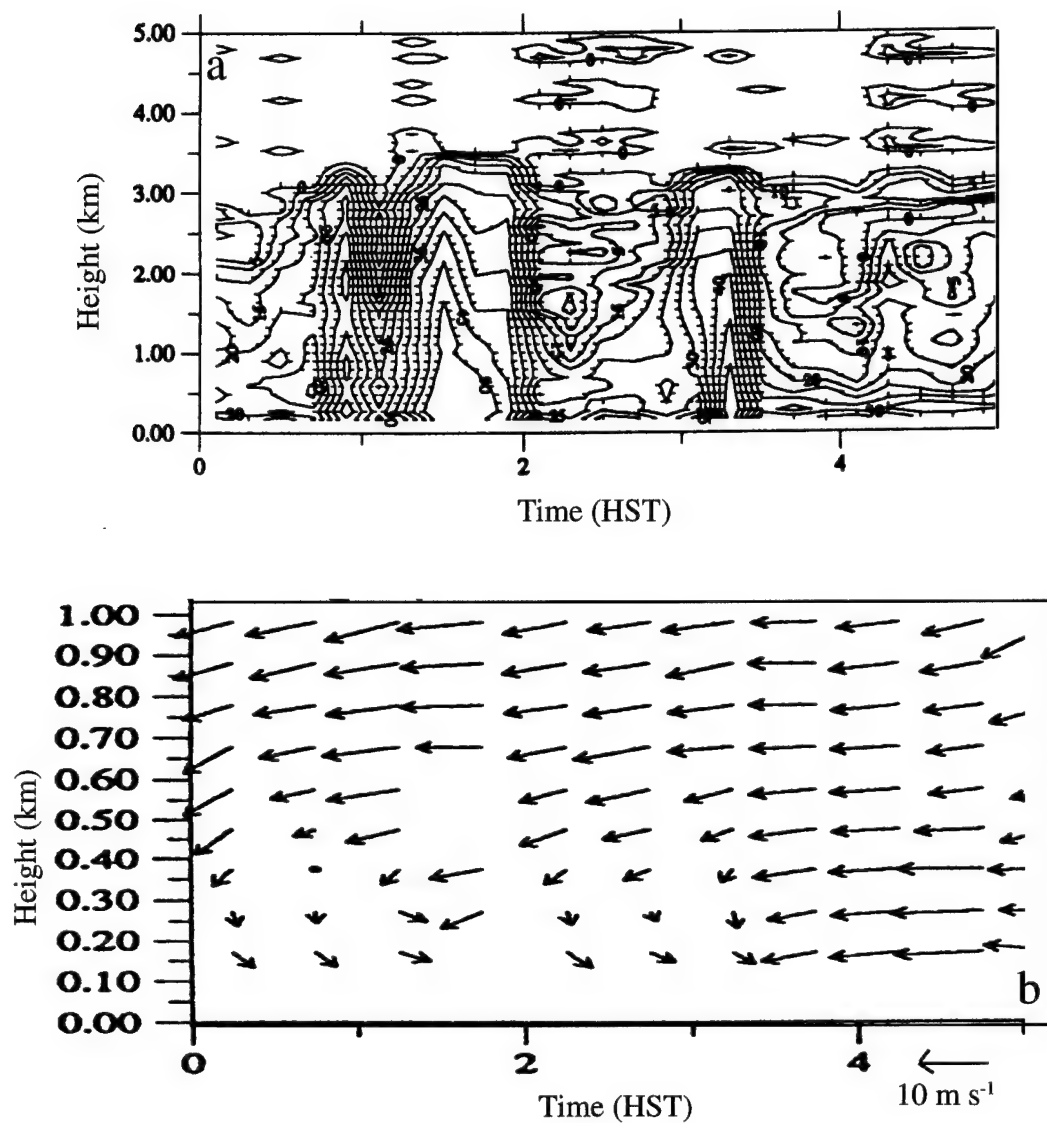
Fig. 4.18   Data from NOAA boundary layer profiler at Paradise Park on 8 August 1990 from 0000-0500 HST. (a) 12 minute average reflectivity (dBZ) every 5 dBZ, and (b) 30 minute average winds (m s⁻¹).
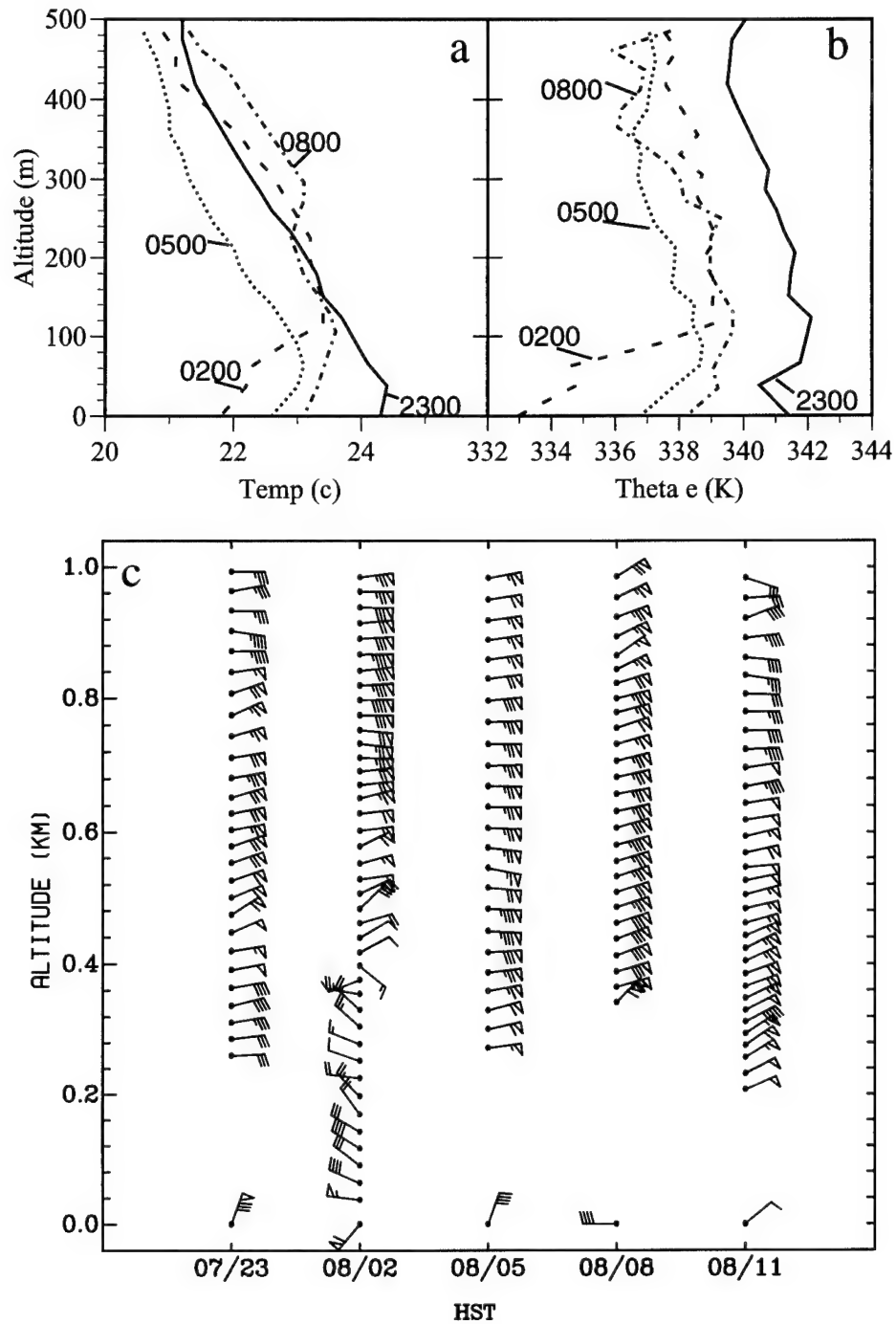
Fig. 4.19 Hilo soundings on 7-8 August 1990, (a) temperature (°C) and (b) equivilent potential temperature (K) at 2300 HST (solid line), 0200 HST (dahed line), 0500 HST (dotted line), 0800 HST (dash-dotted line); (c) wind profiles (m s⁻¹).

76

Fig. 4.20   Same as Fig. 4.6 but at 0600 HST.
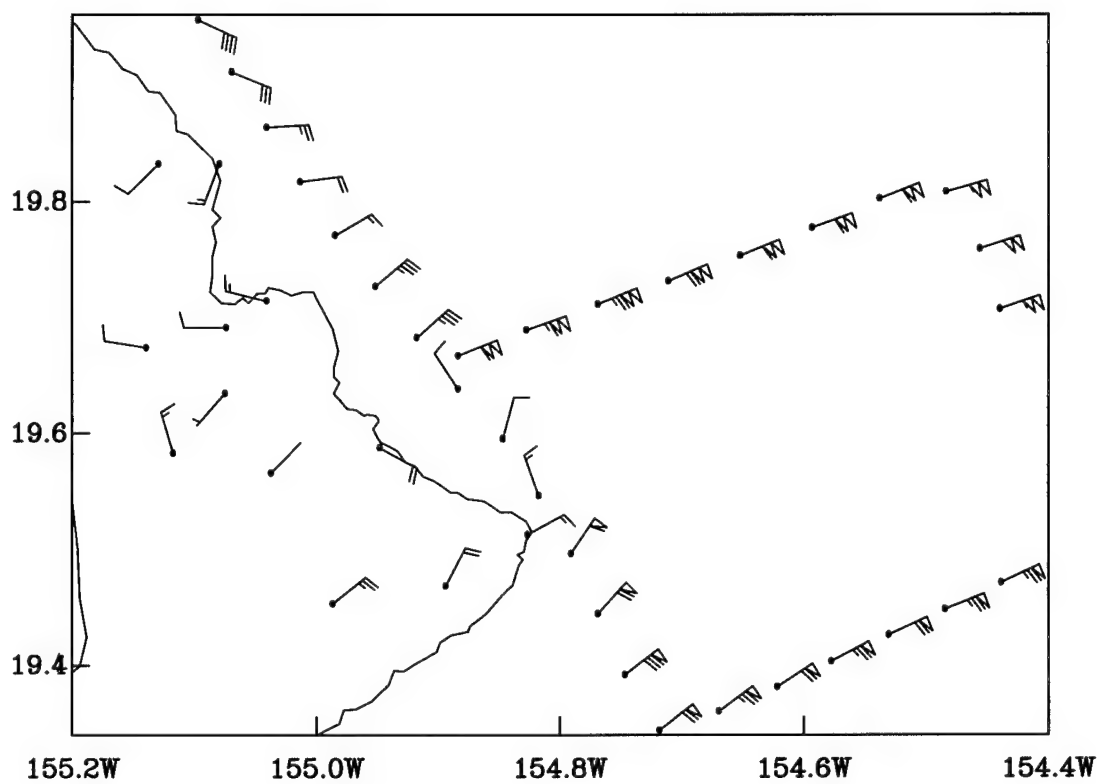
Fig. 4.21 Aircraft measured winds between 150-200 m between 0500-0545 HST. PAM data same as Fig. 4.1 but at 0515 HST.
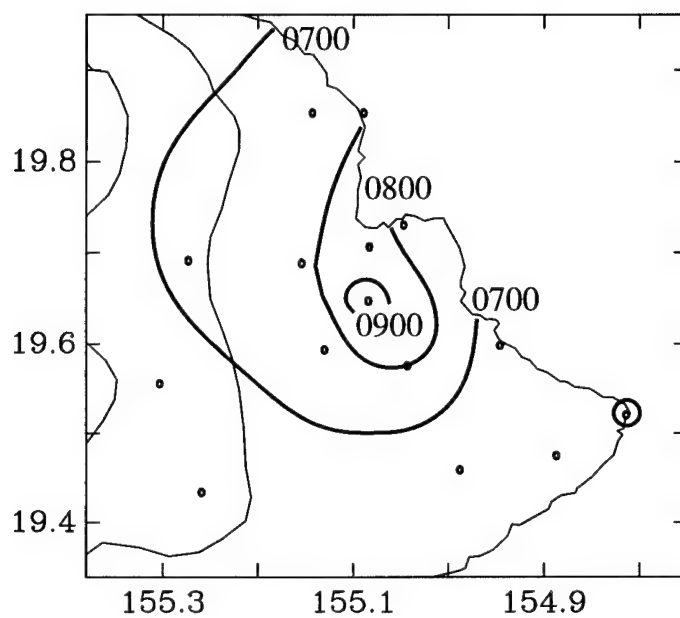
Fig. 4.22 Isochrone analysis of onset of upslope flow on 8 August. Time is HST. Circle indicates station with no windshift.
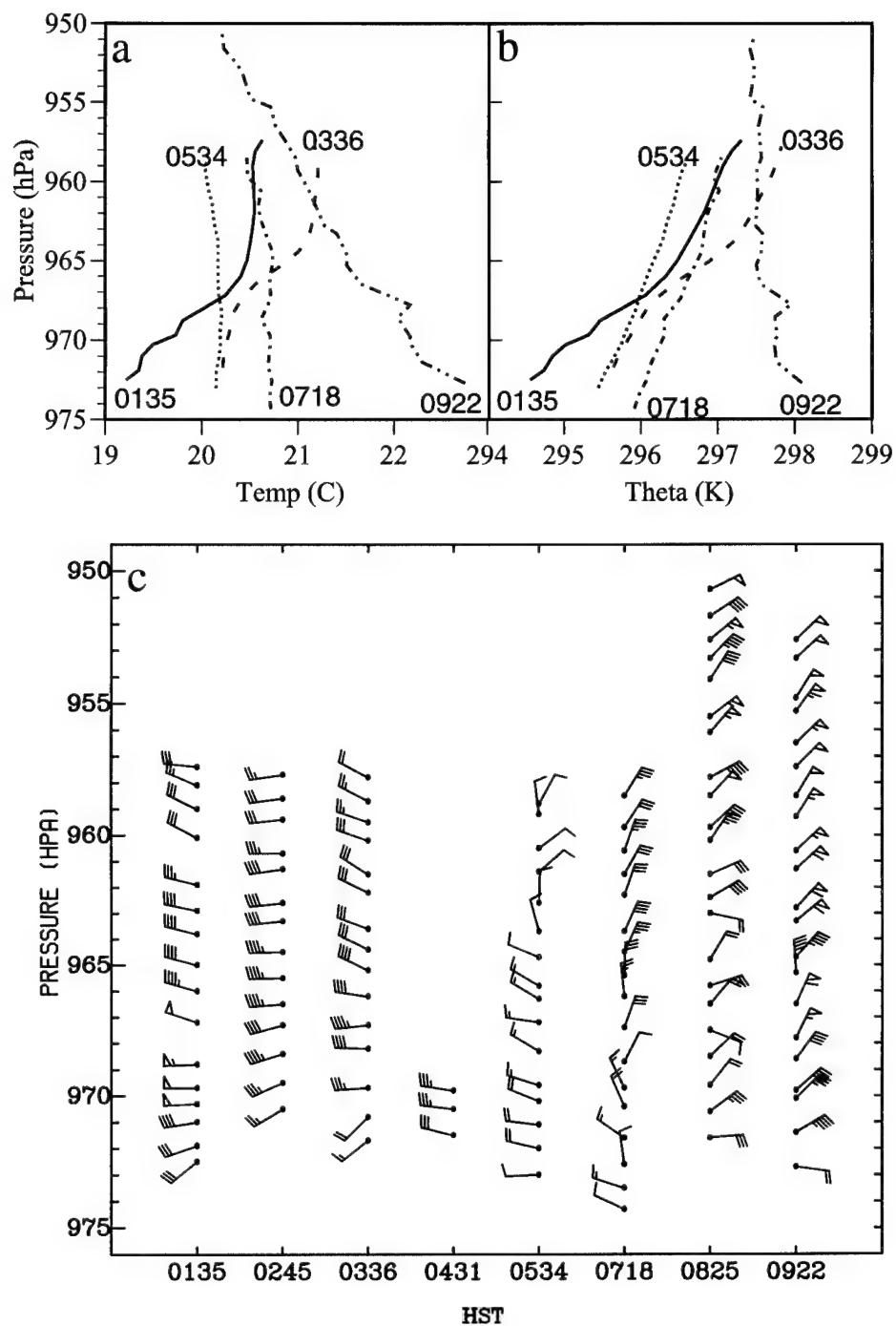
Fig. 4.23 Same as Fig. 4.9 but for 8 August 1990, (a) temperature (°C) and (b) potential temperature (K) at 0135 HST (solid line), 0336 HST (dahed line), 0534 HST (dotted line), 0718 HST (dash-dotted line), 0922 HST (dash-double dotted line); (c) wind profiles (m s⁻¹).
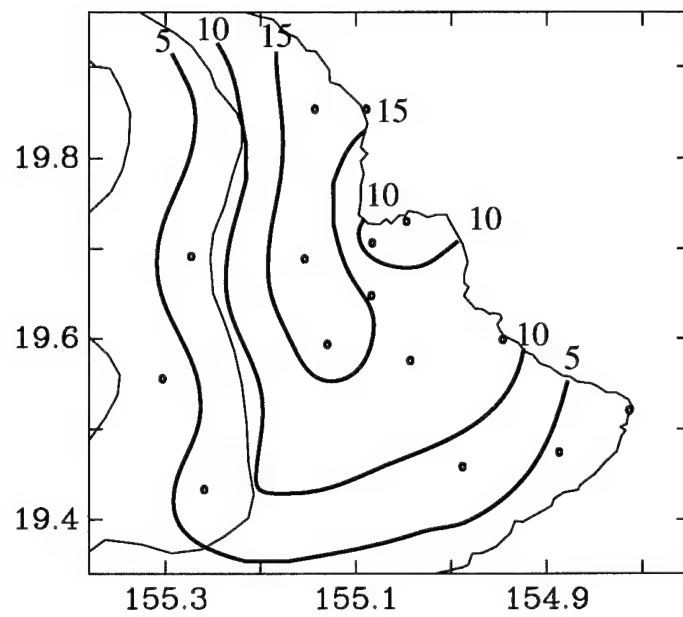
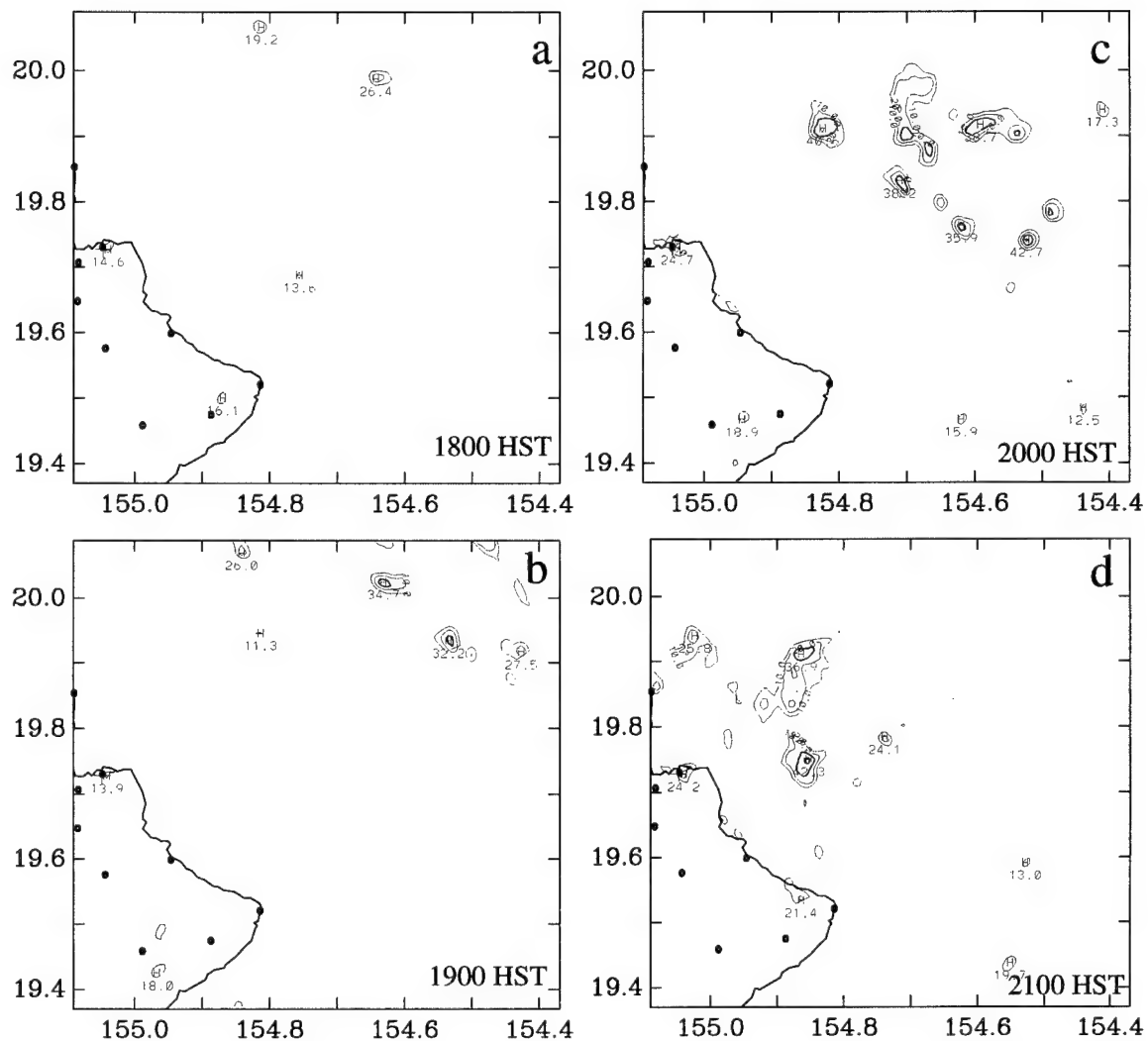Fig. 5.1   Rainfall accumulation (mm) between 2300 HST on 7 August 1990 to 0700
HST on 8 August 1990.

Fig. 5.2   CP4 reflectivity at 0.5° elevation angle for 7 August 1990 at (a) 1800 HST; (b)
1900 HST; (c) 2000 HST; and (d) 2100 HST. Radar reflectivity contours
every 10 dBZ starting at 10 dBZ. Contour line thicker for reflectivity greater
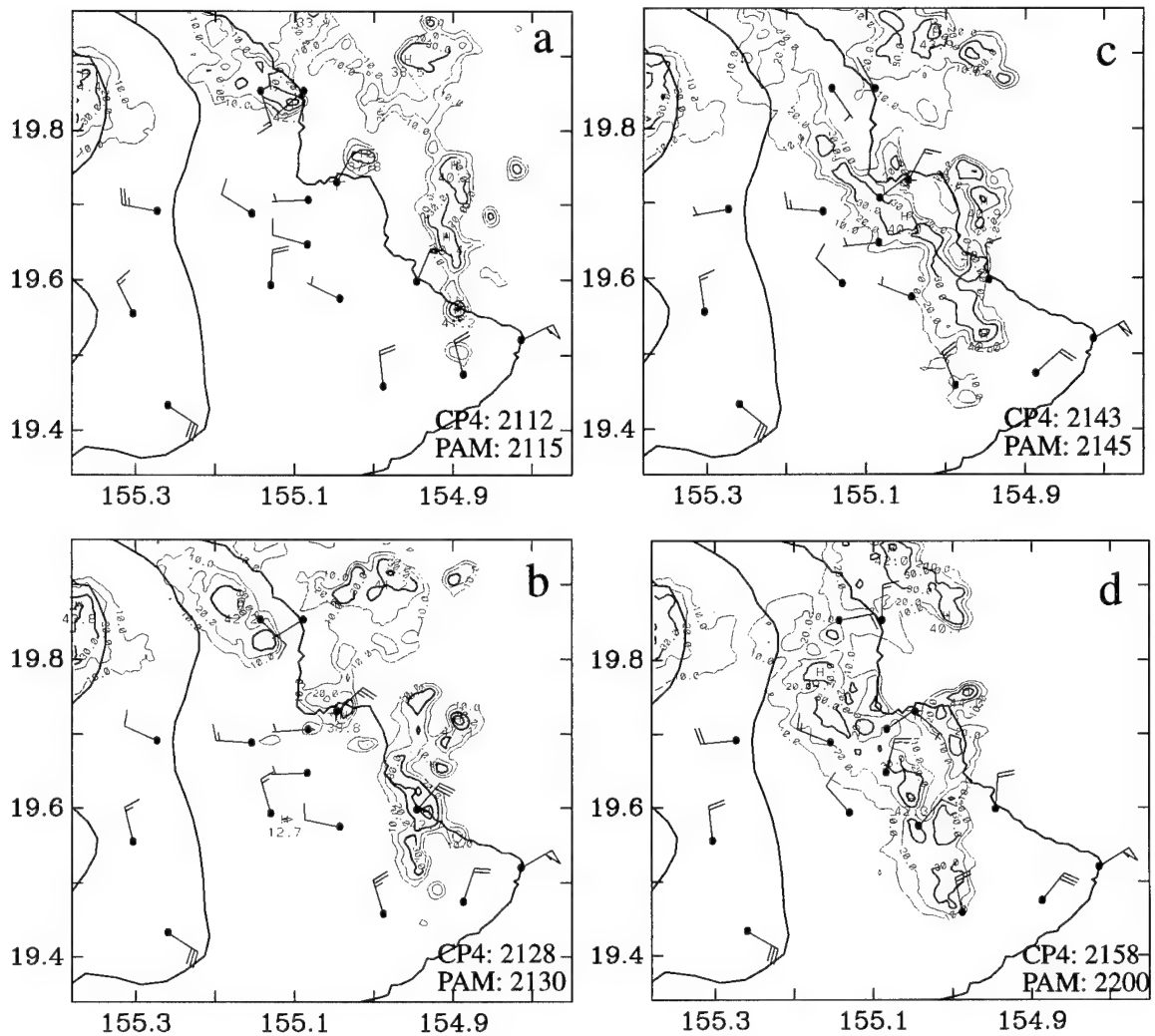than 30 dBZ.

82

Fig. 5.3   PAM winds and CP4 reflectivity at 4.5° elevation angle for 7 August 1990 at
(a) 2115 HST; (b) 2130 HST; (c) 2145 HST; and (d) 2200 HST. Radar
reflectivity contours every 10 dBZ starting at 10 dBZ. Contour line thicker for
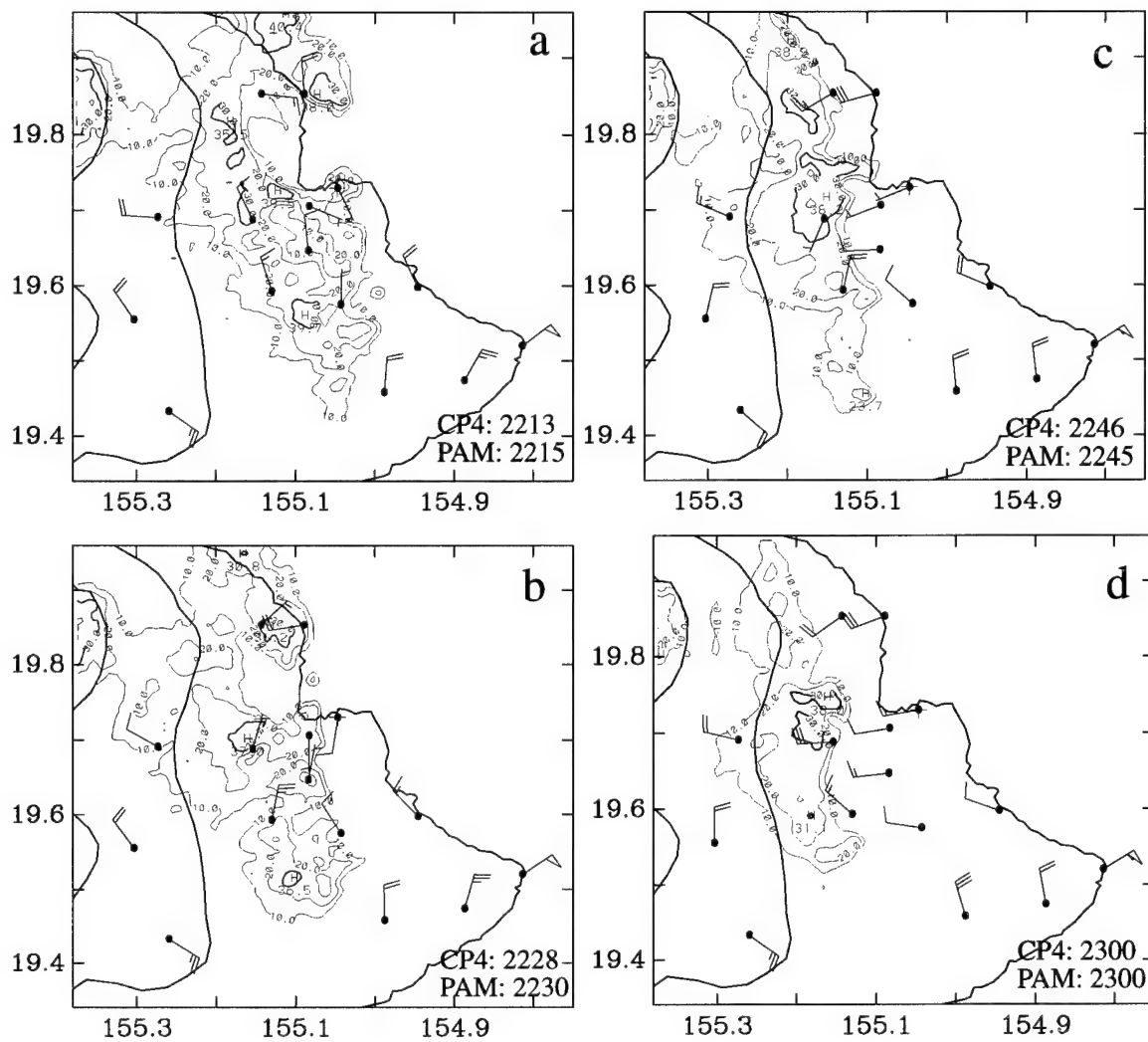reflectivity greater than 30 dBZ.

83

Fig. 5.4   Same as Fig. 5.3 for 7 August 1990 (a) 2215 HST; (b) 2230 HST; (c) 2245 HST; and (d) 2300 HST.
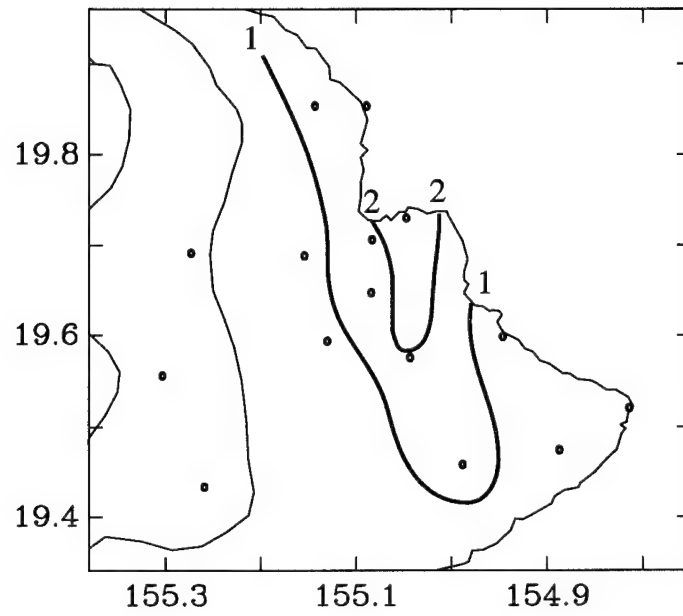
84

Fig. 5.5   Rainfall accumulation (mm) between 2100-2300 HST on 7 August 1990.
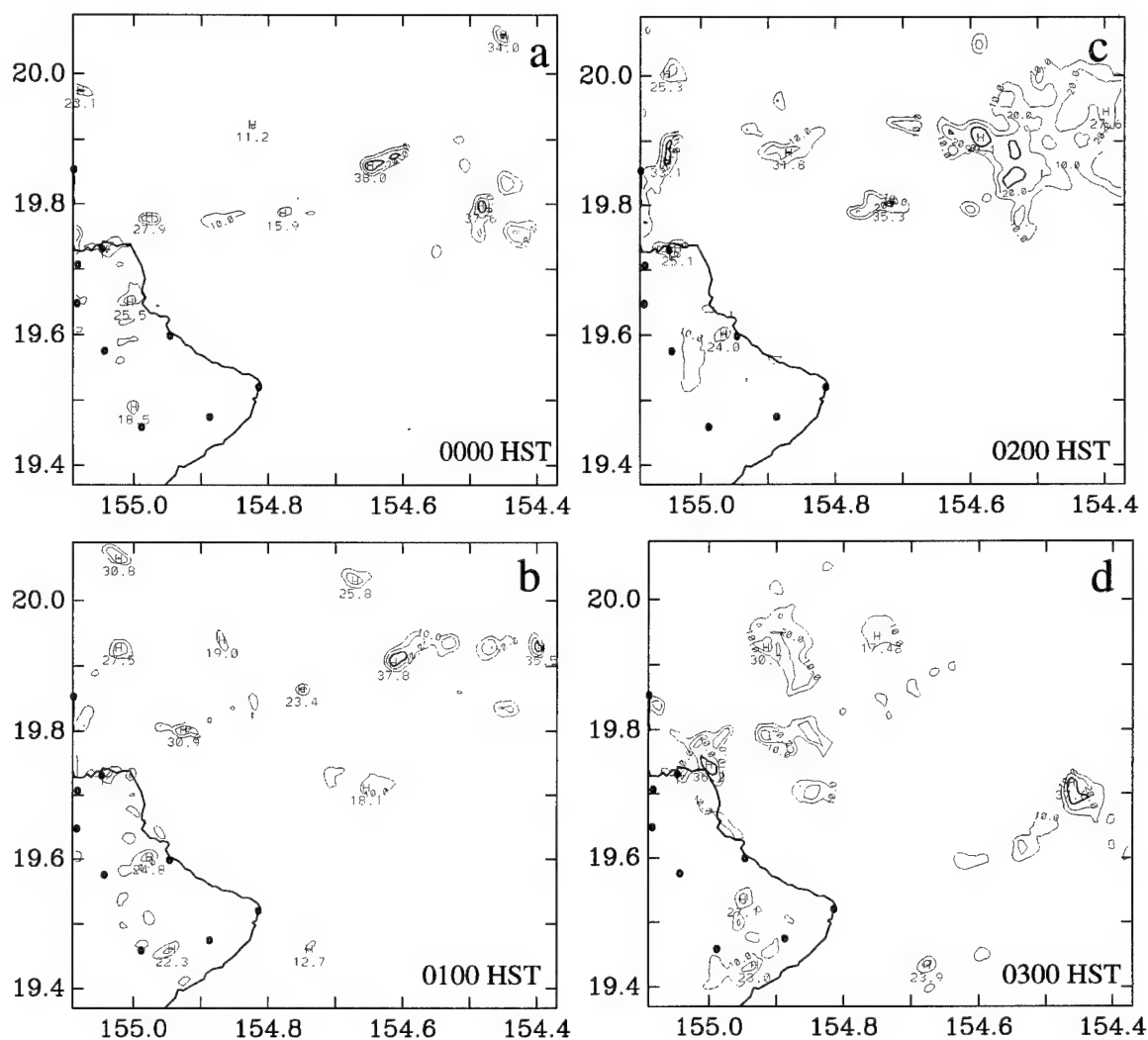
85

Fig. 5.6   Same as Fig. 5.2 for 8 August 1990 at (a) 0000 HST; (b) 0100 HST; (c) 0200
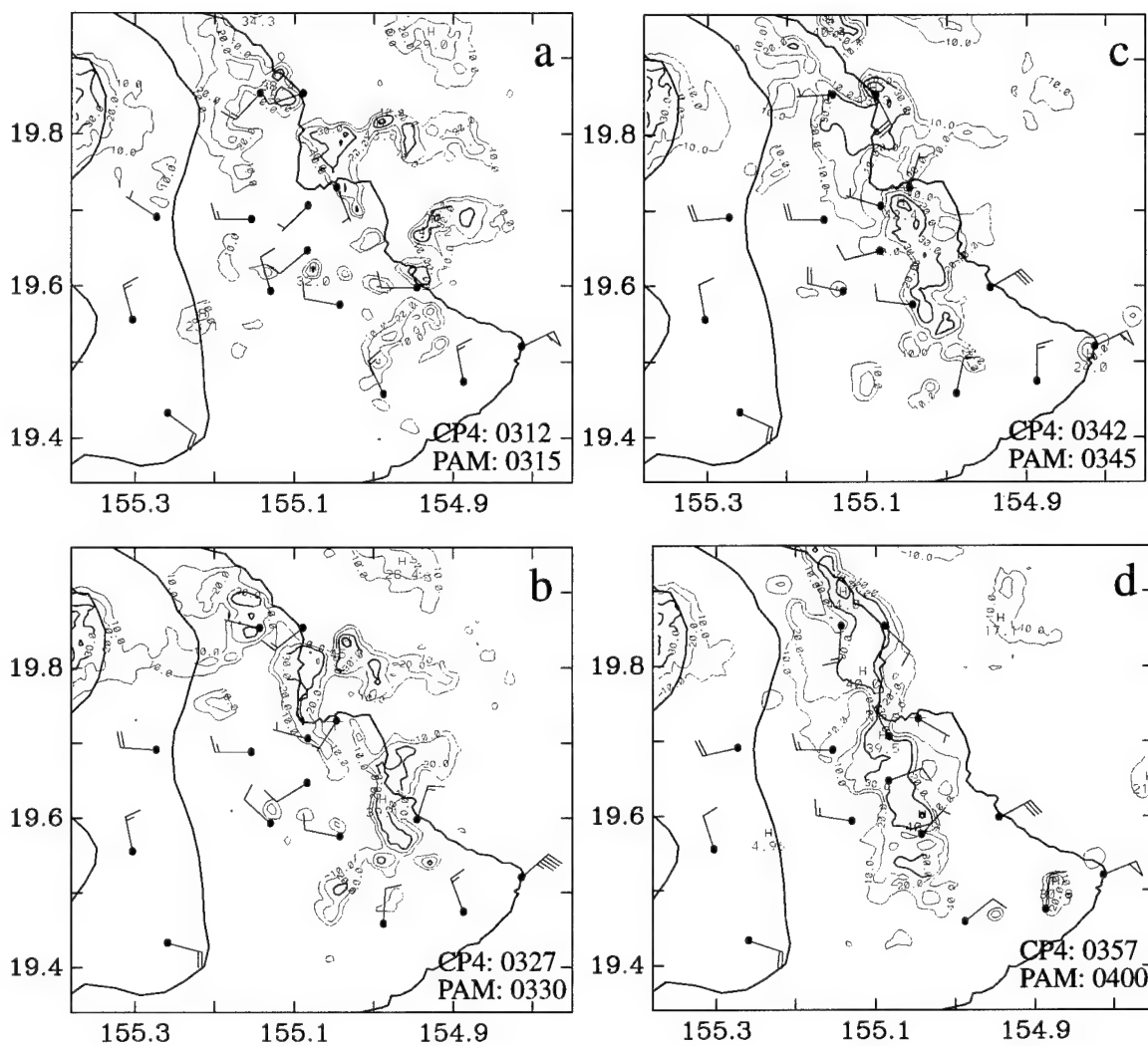HST; and (d) 0300 HST.

Fig. 5.7   Same as Fig. 5.3 for 8 August 1990 at (a) 0315 HST; (b) 0330 HST; (c) 0345
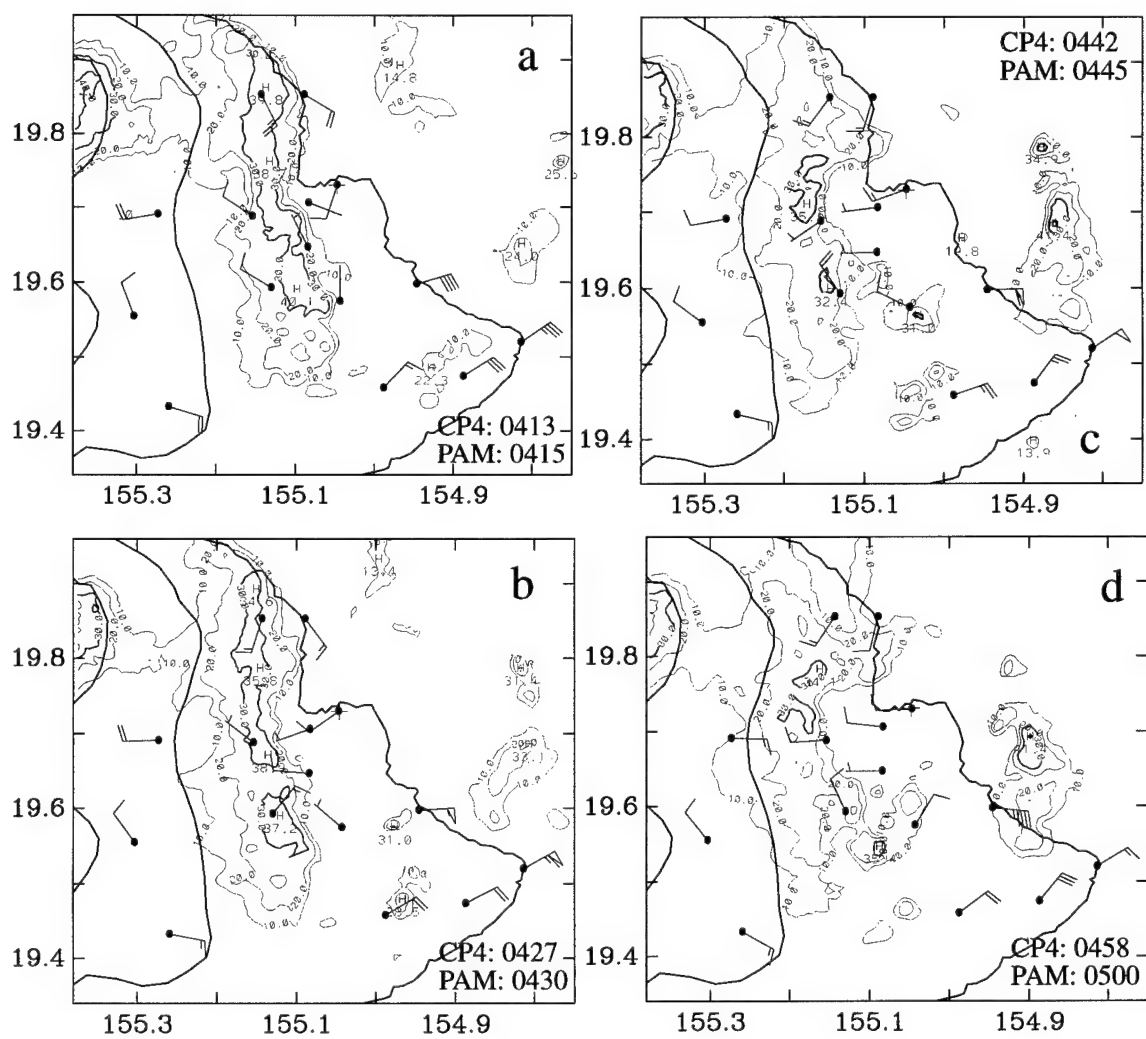HST; and (d) 0400 HST.

Fig. 5.8   Same as Fig. 5.3 for 8 August 1990 at (a) 0415 HST; (b) 0430 HST; (c) 0445
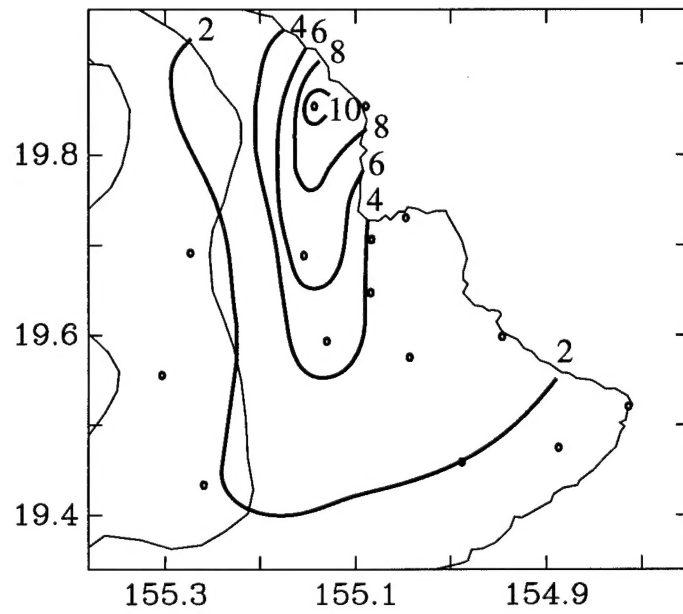HST; and (d) 0500 HST.

88

Fig. 5.9 Rainfall accumulation (mm) between 0300-0500 HST on 8 August 1990.

REFERENCES

Ahnert, P. R., 1990: Functional precision of National Weather Service upper air measurements using the VIZ Manufacturing Co. "B-Sonde," Test and Evaluation Branch Report, 27 pp, draft.

Carbone, R. E., W. A. Cooper, and W. C. Lee, 1994: On the forcing of flow reversal along the windward slopes of Hawaii. *Mon. Wea. Rev.*, **123**, 3466-3480.

Chen Y.-L., and A. J. Nash, 1994: Diurnal variations of surface airflow and rainfall frequencies on the island of Hawaii. *Mon. Wea. Rev.*, **122**, 34-56.

_____and J. J. Wang, 1994: Diurnal variations of surface thermodynamic fields on the island of Hawaii. *Mon. Wea. Rev.*, **122,** 2125-2138.

_____ and _____, 1995: The effects of precipitation on the surface temperature and airflow over the island of Hawaii. *Mon. Wea. Rev.*, **123**, 681-694.

_____and J. Feng, 1995: The influences of inversion height on precipitation and airflow over the island of Hawaii. *Mon. Wea. Rev.*, **123,** 1660-1676.

Eber, L. E., 1957: Upper air and surface wind observations in Project Shower. *Tellus*, 9, 558-568.

Feng, J., and Y. L. Chen, 1996: The evolution of downslope flow on the island of Hawaii during 10 August, 1990. *Mon. Wea. Rev.*, (Submitted).

Garrett, A. J., 1980: Orographic cloud over the eastern slopes of Mauna Loa Volcano, Hawaii, related to insolation and wind. Mon. Wea. Rev., **108**, 931-941.

Grindinger, C. M., 1992: Temporal variability of the trade wind inversion: Measured with a boundary layer vertical profiler. M.S. thesis, Department of Meteorology, University of Hawaii, 93 pp.

Hawaiian Rainband Project (HaRP) Data Catalog, 1990: National Center for Atmospheric Research Report, 200 pp.

Larson, R. N., 1978: Summer trade wind rainfall in the Hawaiian Islands. M.S. thesis, Department of Meteorology, University of Hawaii, 85 pp.

Leopold, L. B., 1949: The interaction of trade wind and sea breeze, Hawaii. *J. Meteor.*, **8**, 533-541.

Lavoie, R. L., 1967: Air motions over the windward coast of the island of Hawaii. *Tellus*, **19**, 354-358.

Mendonca, B. G., 1969: Local wind circulation on the slope of Mauna Loa. *J. Appl. Meteor.*, **8**, 533-541.

Oke, T. R., 1987: *Boundary Layer Climates.* Routledge, 435 pp.

Rasmussen, R. M., and P. K. Smolarkiewicz, 1993: On the dynamics of Hawaiian cloud bands. Part III: Local aspects. *J. Atmos. Sci.*, **50**, 1560-1572.

_____, and _____, and J. Warner, 1989: On the dynamics of Hawaiian cloud bands: Comparison of model results with observations and island climatology. *J. Atmos. Sci.*, **46**, 1589-1608.

Schroeder, T. A., 1981: Characteristics of local winds in northeast Hawaii. *J. Appl. Meteor.*, **20**, 874-81.

Smolarkiewicz, P. K., R. M. Rasmussen, and T. L. Clark, 1988: On the dynamics of Hawaiian cloud bands: Island forcing. *J Atmos. Sci.*, **45**, 1872-1905.

Takahashi, T., 1977: Rainfall at Hilo, Hawaii. *J. Meteor. Soc. Jpn*, **55**, 121-129.

Wang, J.-J., 1995: Circulations induced by the island of Hawaii and their interaction with trade-wind rainbands. Ph.D. dissertation, Department of Meteorology, University of Hawaii, 189 pp.

Wang J.-J., and Y. L. Chen, 1995: Characteristics of near-surface winds and thermal profiles on the windward slopes of Hawaii. *Mon. Wea. Rev.*, **123**, 3481-3501.

_____, and _____, 1996: Case study of trade-wind showers on the island of Hawaii. *Mon. Wea. Rev.*, (Accepted)